

1 **Variability of the infrared complex refractive index of African**
2 **mineral dust: experimental estimation and implications for**
3 **radiative transfer and satellite remote sensing**

5 C. Di Biagio^{1,*}, H. Boucher², S. Caquineau², S. Chevaillier¹, J. Cuesta¹, and P. Formenti¹

6 ¹ LISA, UMR CNRS 7583, Université Paris Est Créteil et Université Paris Diderot, Institut
7 Pierre Simon Laplace, Créteil, France

8 ² IPSL/LOCEAN, UMR 7159-IRD-CNRS-UPMC-MNHN, Institut de Recherche pour le
9 Développement, Bondy, France

10 Correspondence to: C. Di Biagio (claudia.dibiagio@lisa.u-pec.fr)

11 **Abstract**

12 Experimental estimations of the infrared refractive index of African mineral dust have been
13 retrieved from laboratory measurements of particle transmission spectra in the wavelength
14 range 2.5-25 μm . Five dust samples collected at Banizoumbou (Niger) and Tamanrasset
15 (Algeria) during dust events originated from different Western Saharan and Sahelian areas
16 have been investigated. The obtained real (n) and imaginary (k) parts of the refractive index
17 for the different dust samples vary in the range 1.1-2.7 and 0.05-1.0, respectively, and appear
18 to be strongly sensitive to the mineralogical composition of the particles, especially in the 8-
19 12 μm and 17-25 μm spectral intervals. Dust absorption is controlled mainly by clays
20 (kaolinite, illite, smectite), and, in minor fraction, by quartz and Ca-rich minerals (e.g.,
21 calcite, gypsum). Significant differences are obtained when comparing our results with
22 existing experimental estimations available in the literature, and with the values of the OPAC
23 (Optical Properties of Aerosols and Clouds) database. The different datasets appear
24 comparable in magnitude, with our values of n and k falling in the range of variability of past
25 studies. However, literature data fail in accurately reproducing the spectral signatures of main
26 minerals, in particular clays, and they significantly overestimate the contribution of quartz.
27 Furthermore, the real and the imaginary parts of the refractive index from part of literature
28 studies are found not to verify the Kramers-Kronig relations, thus resulting theoretically
29 incorrect. The comparison between our results, from Western Africa, and literature data, from
30 different locations in Europe, Africa, and the Caribbean, nonetheless, confirms the expected
31

32 large variability of the dust infrared refractive index. This highlights the necessity for an
33 extended systematic investigation of dust properties at infrared wavelengths.

34 For the five analysed dust samples, aerosol intensive optical properties relevant to radiative
35 transfer (mass extinction efficiency, k_{ext} , single scattering albedo, ω , and asymmetry factor,
36 g), have been calculated, by using the Mie theory, based on the estimated refractive index and
37 measured particle size distribution. The optical properties show a large sample-to-sample
38 variability, with k_{ext} , ω , and g varying in the range 0.05-0.35, 0.25-1.0, and 0.05-0.75. This
39 variability is expected to significantly impact satellite retrievals of atmospheric and surface
40 parameters (e.g. from IASI) and estimates of the dust radiative forcing.

41

42 1. Introduction

43 Mineral dust is one of the most abundant aerosol species in the atmosphere and strongly
44 contributes to the total aerosol content (Textor et al., 2007; Huneeus et al., 2012). The arid
45 and semi-arid regions of West Africa, i.e. the Sahara and the Sahel, account for more than
46 60% of the total annual dust emission, and are by far the most significant sources of mineral
47 dust at the global scale (Prospero et al., 2002; Laurent et al., 2008; Ginoux et al., 2012). Once
48 emitted, African dust is transported for thousands of kilometres across the Atlantic Ocean
49 (e.g., Ben-Ami et al., 2009 and 2010) and the Mediterranean basin (e.g., Israelevich et al.,
50 2002), thus affecting the environment at intercontinental distances.

51 Mineral dust directly affects the planetary radiative balance by absorption and scattering of
52 radiation (Sokolik and Toon, 1996). Due to their high atmospheric load, dust aerosols are
53 observed to exert a significant radiative effect both close to source regions and in transport
54 areas (Haywood et al., 2003; Highwood et al., 2003; Di Biagio et al., 2010). As a
55 consequence of the effect on radiation, mineral dust impacts the atmospheric thermal
56 structure and stability (Kishcha et al., 2003; Heinold et al., 2008), with possible effects on
57 cloud formation and properties (Rosenfeld et al., 2001; Klüser and Holzer-Popp, 2010), as
58 well as on atmospheric photochemical reactions (Casasanta et al., 2011). The implications on
59 the hydrological cycle, in particular, are of great relevance for water-stressed semi-arid areas,
60 as it is the case of the Sahel, mainly in relation to possible feedback mechanisms on dust
61 emission in these regions (Carlsaw et al., 2010).

62 Due to its characteristic mineralogical composition and extended particle size spectrum (from
63 tenths of nanometers to tenths of micrometers), mineral dust effectively interacts with both

64 the solar and the terrestrial infrared radiation fields (Ackerman and Chung, 1992; Hsu et al.,
65 2000; Brindley and Russell, 2009). In terms of magnitude, the instantaneous solar effect is
66 considerably larger than the infrared one, which generally becomes relevant only for very
67 high dust amounts (e.g., Slingo et al., 2006). However, while the solar contribution is
68 effective only during daytime, the infrared term acts throughout the 24-hours, thus on a daily
69 basis it may compensate for a large fraction of the diurnal shortwave perturbation (e.g., di
70 Sarra et al., 2011). The infrared term needs therefore to be taken into account in order to
71 estimate the whole dust radiative effect.

72 The interaction of atmospheric dust with infrared radiation has also been shown to
73 significantly affect the interpretation of remote sensing data. In particular, several key
74 climatic parameters, such as the atmospheric temperature profile, sea surface temperature,
75 and greenhouse gases concentration, are derived from satellite measurements over
76 narrowband infrared channels (MODIS, Moderate Resolution Imaging Spectroradiometer;
77 SEVIRI, Spinning Enhanced Visible and Infrared Imager; AVHRR, Advanced Very High
78 Resolution Radiometer; HIRS, High-resolution Infrared Radiation Sounder; AIRS,
79 Atmospheric Infrared Sounder; IASI, Infrared Atmospheric Sounding Interferometer).
80 Misinterpretations of the data occur when the infrared radiative effect of dust is not
81 accurately taken into account within satellite inversion algorithms (e.g., Ackerman, 1997;
82 Sokolik, 2002; DeSouza-Machado et al., 2006). On the other hand, the dust infrared signature
83 obtained in satellite data, especially in the 8-12 μm window region, is used to detect the
84 presence and estimate the properties of dust from space (Legrand et al., 2001; Pierangelo et
85 al., 2004; Klüser et al., 2011; Banks and Brindley, 2013; Capelle et al., 2013).

86 Still, very large uncertainties persist in the estimation of the dust infrared radiative effect
87 (Haywood et al., 2005; Balkanski et al., 2007; Bierwirth et al., 2009). One of the main causes
88 for this is the poor knowledge of the dust optical properties in this portion of the spectrum
89 (e.g., Wang et al., 2006). Dust infrared optical properties, in fact, cannot be directly measured
90 by in situ instruments, and also their estimation based on ground-based or satellite remote
91 sensing observations is difficult, due to the fact that the aerosol signature is partly covered by
92 that of main atmospheric constituents (water vapour, CO_2) and that a priori knowledge of the
93 investigated optical properties is often required by inversion algorithms. So, dust infrared
94 optical properties are generally estimated through an alternative approach, which consists in
95 calculating them based on the knowledge of the physico-chemical properties of particles, i.e.
96 composition, size distribution, and shape (Levin and Lindberg, 1979; Highwood et al., 2003).

97 In this sense, the complex refractive index, $m = n - ik$, the parameter linking the physico-
98 chemical and the optical properties of aerosols, remains a major unknown (e.g., Sokolik et al.,
99 1993; Clauquin et al., 1998).

100 The dust complex refractive index is mainly controlled by particle mineralogical composition
101 (Patterson et al., 1981; Sokolik et al., 1998). Dust is composed of several minerals, such as
102 clays (kaolinite, illite, smectite, chlorite), quartz, Ca-rich carbonates (calcite, dolomite) and
103 sulphates (gypsum), feldspars (orthose, albite), and iron and titanium oxides, each
104 characterised by specific lattice vibrational-rotational transitions, therefore by its own
105 spectral refractive index in the infrared (Sokolik and Toon, 1999). Consequently, the
106 magnitude and the spectral dependence of the dust complex refractive index depend on the
107 abundance and state of mixing (internal or external) of its main constituents (e.g.,
108 Mishchenko et al., 2004). Due to the diverse soil mineralogy of the different source areas
109 (Clauquin et al., 1999), the composition of dust aerosols varies depending on the region of
110 origin (e.g., Caquineau et al., 2002). The proportion between the different minerals at
111 emission also critically depends on the surface wind speed of erosion, which also determines
112 their size distribution (Gomes and Gillette, 1993; Marticorena and Bergametti, 1995). Quartz,
113 feldspars, and Ca-rich species are generally more abundant in the coarse mode component,
114 while clays dominate the fine fraction (e.g., Pye et al., 1987; Kandler et al., 2009). The
115 mineralogical composition of dust then changes rapidly after emission mainly as a
116 consequence of the progressive loss of coarse particles due to gravitational settling (Schütz et
117 al., 1981; Maring et al., 2003). This process reduces the abundance of quartz, feldspars, and
118 Ca-rich species in the dust aerosol, thus yielding clay richer particles. Also, when travelling
119 over marine or polluted environments, the composition of dust may be additionally modified
120 due to the interaction with other aerosol types (e.g., sea salts, soot) or atmospheric gases (e.g.,
121 nitrates, sulphates) (Formenti et al., 2011). As a consequence of all these processes, the
122 complex refractive index of mineral dust is expected to vary as a function of the source
123 region and during atmospheric transport. The complete characterization of this variability is
124 necessary to evaluate the magnitude of the dust radiative effect along its whole atmospheric
125 lifecycle.

126 A very few number of studies, from a limited number of geographical locations worldwide
127 (e.g., Germany, Barbados, Niger), have investigated the complex refractive index of dust
128 aerosols at infrared wavelengths (Volz, 1972 and 1973; Fisher, 1976; Patterson, 1981;
129 Fouquart et al., 1987; see also Sokolik et al. (1993) and (1998) and references therein).

130 Hence, to date, the natural variability of the dust infrared refractive index remains not
131 represented. Moreover, some degrees of uncertainties remain on the accuracy and
132 representativeness of these few data. In all of these studies, in fact, the refractive index of
133 dust is estimated by means of the spectroscopy pellet technique. This approach consists in
134 dispersing the aerosol particles in a matrix of transparent material, e.g. potassium bromide
135 (KBr), which is then pressed to form a homogeneous pellet. A typical fraction of 0.1% of
136 dust particles is dispersed in a total of 100-300 mg of KBr. The reflectance or transmission
137 spectrum of the pellet is then measured and analysed by means of an appropriate optical
138 theory to retrieve the complex refractive index of the particles. The pellet technique presents
139 however several limitations which make it not fully adapted to investigate aerosols. At first,
140 this technique requires one to manipulate the aerosol sample, mixing it with KBr, and then to
141 press the mixture to form the pellet. These operations may modify the physico-chemical
142 properties of the particles, thus reducing the representativeness of the analysed samples
143 compared to natural airborne conditions. In particular, the aerosol size distribution, as well as
144 the morphology of the particles, may be affected by these modifications, mainly due to the
145 pressing during pellet production. Moreover, the fact of dispersing a very small quantity of
146 aerosol (0.1%) in the KBr matrix determines a strong suppression of the aerosol scattering
147 signal, which becomes almost negligible compared to that from the matrix itself. As a
148 consequence, mainly the absorption component of the extinction is measured with the pellet
149 technique, with a strong underestimation of the scattering fraction. This aspect is particularly
150 important for dust particles, for which scattering is estimated to significantly contribute to the
151 atmospheric infrared extinction (Dufresne et al., 2002). Despite these limitations and
152 uncertainties, nonetheless, pellet spectroscopy data represent nowadays the only available
153 references for dust infrared optical properties, and are used as the main basis for global
154 aerosol databases such as OPAC (Optical Properties of Aerosols and Clouds; Hess et al.,
155 1998) and GADS (Global Aerosol Data Set; Koepke et al., 1997).

156 In this study we apply the spectroscopy pellet technique to provide new experimental
157 estimates of the infrared complex refractive index of dust aerosols. Natural particle samples
158 from Western Sahara and the Sahel, some of strongest sources at the global scale (Ginoux et
159 al., 2012), have been considered. The paper has two main objectives: (i) to test the sensitivity
160 of the dust infrared refractive index to the physico-chemical properties of particles, in
161 particular to the mineralogy. We want to show that, also at the small scale (Western Africa),
162 there is a significant variability of the dust refractive index as a function of particle properties

163 that past studies are only in part able to detect; (ii) to show the importance of this variability
164 on radiative forcing calculations and satellite remote sensing. The dust refractive index has
165 been estimated in this study from spectroscopy pellet transmission measurements by applying
166 an experimental procedure and a retrieval scheme mostly consistent with those of past
167 literature studies (see also Sect. 2.1). We have made this choice, aware of the limits and
168 uncertainties of the spectroscopy technique discussed above, to simplify the comparison
169 between past and new data, thus allowing an easier evaluation of the dust refractive index
170 variability.

171 Dust samples analysed here have been collected during the AMMA 2006 campaign (African
172 Monsoon Multidisciplinary Analysis; Redelsperger et al., 2006) at the ground-based super-
173 sites of Banizoumbou (13.5°N, 2.6°E, 250 m a.s.l.), located in a remote area ~60 km east of
174 Niamey in Niger (Rajot et al., 2008), and Tamanrasset (22.8°N, 5.5°E, 1370 m a.s.l.), in the
175 heart of the Hoggar massif in South Algeria (Cuesta et al., 2008). Five different dust cases
176 were selected based on their different origin and mineralogical composition, three from the
177 Banizoumbou site, and two from Tamanrasset. As here we want to focus on the refractive
178 index variability near source regions, the five cases have been chosen to be representative of
179 local emission episodes or of dust at most after 1-2 days of atmospheric transport. A
180 summary of the main information for the selected Banizoumbou and Tamanrasset dust events
181 is reported in Table 1. A more detailed discussion of the five dust episodes and identification
182 of their different source region is provided in Appendix A.

183 The paper is organised as follows: In Sect. 2 we present the measurements used in this
184 analysis, the experimental method, and the main algorithm for complex refractive index
185 estimation. The physico-chemical properties obtained for the considered samples are
186 discussed in Sect. 3. Sect. 4 is then dedicated to the presentation and discussion of the
187 spectroscopy measurements and complex refractive index results. The effect of the variability
188 of the refractive index and size distribution on the optical properties of dust, as well as its
189 possible implications on radiative transfer and satellite remote sensing, is investigated in Sect.
190 5. The main conclusions of this study are discussed in Sect. 6.

191

192 **2. Measurements and methods**

193 Aerosol samples have been collected at the two sites of Banizoumbou and Tamanrasset on
194 47-mm polycarbonate Nuclepore filters (nominal pore size 0.4 μm). The sampling time for

195 the different cases (see Table 1) varied between a few hours to 1-2 days, depending on the
196 aerosol concentration and the duration of the event. Dust particles deposited on filters have
197 been analysed to obtain their bulk mineralogical composition. Then the infrared transmission
198 spectra have been measured on the samples of collected dust to estimate their complex
199 refractive index. The number size distribution of dust particles in the diameter range 0.3-20
200 μm was measured during filter sampling by means of a Grimm Optical Particle Counter
201 (OPC, model 1.108). Full details on spectroscopy measurements and algorithm for complex
202 refractive index estimation, dust filter chemical analyses, and procedures for size distribution
203 data corrections are provided in the next paragraphs.

204

205 **2.1 Infrared spectroscopy and dust complex refractive index estimation**

206 Transmittance spectra (T) of collected dust particles have been recorded in the wavelength
207 range 2.5–25 μm (4000-400 cm^{-1} wavenumber) at 2 cm^{-1} resolution by means of a Bruker
208 Optics Equinox 55 FT-IR spectrometer. The instrument uses a Globar source, with a KBr
209 beamsplitter and a deuterated triglycine sulphate (DTGS) detector. The infrared transmission
210 spectroscopy has been performed by means of the usual pellet technique (i.e., Volz, 1972;
211 Mooney and Knacke, 1985) using KBr as transparent matrix in which dust grains have been
212 dispersed.

213 Dust particles collected on Nuclepore membranes need to be extracted from filters to mix
214 with the KBr powder and then to produce the pellets. As discussed in the Introduction, the
215 manipulation of dust particles is a delicate operation and it should be achieved by avoiding as
216 much as possible contaminations or modifications of the sample. We tested different
217 procedures to optimize dust extraction and KBr mixing. Our best obtained experimental
218 protocol is described in the following: (i) *Suspension of dust particles in ethanol solution*. To
219 allow dust particles to detach from the filter membranes, filters are immersed, dust-loaded
220 face downward, in 10-15 ml of ethanol and shaken for ~5-10 minutes at ultrasonic
221 frequencies. The ultrasonic shaking procedure is repeated 2-3 times, until the aerosol has
222 completely left the filter; (ii) *Separation of dust and ethanol*. The dust-ethanol suspension is
223 centrifuged at a speed of 11000 rpm for ~1 hour, thus permitting an effective separation
224 between the liquid (ethanol) and the solid (dust) phases. After centrifugation the dust-ethanol
225 solution is left in vertical position for 1 day to sediment dust particles which had remained in
226 suspension. At this point, having the liquid and solid phases well separated, ~95% of ethanol

227 is removed by pipe aspiration, while the remaining ~5% is left to evaporate for 1 day; (iii)
228 *Dilution of dust particles in the KBr matrix.* Once extracted and transferred in a glass tube,
229 dust particles are weighed and then diluted in a KBr matrix. A high-quality pure potassium
230 bromide (ACROS Organics IR grade) is used. The mass of KBr is set to obtain a total of
231 0.1% of dust in the mixture. Dust and KBr are weighed by means of a Sartorius microbalance
232 (model LE225D) whose maximum sensitivity is 10 μg . The dust-KBr mixture is then
233 mechanically shaken for about 10 minutes to create a homogeneous mixing. The obtained
234 dust-KBr samples and the pure KBr are placed in the oven to dry at the temperature of 100
235 °C for ~12 hours. Passing the samples in the oven does not modify the dust mineralogical
236 composition, as at these temperatures the main effect is water evaporation; (iv) *Pellet*
237 *production.* Each of the 5 dust-KBr mixture samples is softly grounded in agate mortar, in
238 order to slightly change the size of dust grains, and then is pressed under vacuum at the
239 pressure of ~10 Tons cm^{-2} for 1-2 minutes to form a thin pellet. About 150 mg of powder is
240 needed to create a homogeneous pellet of 13 mm diameter (surface 1.33 cm^2) and <1 mm
241 thickness. 3 pure 150 mg KBr pellets are also produced. Then all the pellets are put in the
242 oven at 100 °C for about 1-2 hours until they are used for transmission spectroscopy
243 measurements. This is done to avoid as much as possible water vapour absorption, in
244 particular by the highly hygroscopic KBr. We should expect, as already mentioned, that some
245 of the dust properties, such as the size distribution, aggregation state, or also the morphology
246 of the particles, may partly modify during the pellet production, thus affecting the
247 representativeness of the analysed sample compared to airborne conditions. It should be
248 pointed out, however, that the estimation of the effects of these modifications on the
249 measured spectra is very difficult, and a certain degree of uncertainty on this aspect remains
250 not quantified. All the laboratory operations we have described here are accomplished in
251 clean conditions, i.e., working in a permanently ventilated room, and manipulating the
252 samples in a laminar flow bench.

253 Spectroscopic measurements have been performed on the 5 dust-KBr and the 3 pure KBr
254 samples. Pellets were placed in the spectrometer chamber purged of CO_2 gas and H_2O
255 vapour. A total of 20 and 40 scans were averaged to produce the dust-KBr and the pure KBr
256 spectra, respectively. The 3 spectra of pure KBr have been averaged and used to correct the
257 baseline of dust-KBr. This correction allows removing the signal due to the water vapour or
258 other gases possibly absorbed on the pellet by KBr. Once corrected for the baseline signal,
259 the dust-KBr spectra have been smoothed by performing a 9-point running average.

260 Starting from the measured dust-KBr transmission spectra, the real (n) and the imaginary (k)
261 parts of the dust refractive index have been estimated following the procedure already applied
262 by various authors to investigate Martian dust (e.g., Orofino et al., 1998; Marzo et al., 2004;
263 Marra et al., 2005). The hypotheses at the base of our retrieval scheme, as will be discussed
264 in the following, are coherent with main assumptions performed by most of past studies on
265 dust aerosols available in the literature (e.g., Volz 1972 and 1973; Fouquart et al., 1987).

266 Based on the Beer-Bouguer-Lambert law, the spectral transmittance, $T(\lambda)$, through a thin
267 section of a specific medium is given by:

$$268 \quad \ln\left(\frac{1}{T(\lambda)}\right) = \alpha_{\text{ext}}(\lambda) \cdot x \quad (1)$$

269 where $\alpha_{\text{ext}}(\lambda)$ is the spectral extinction coefficient of the medium and x the pathlength of
270 radiation. In our case the medium is a pellet composed of a matrix of transparent material
271 (KBr) in which a small amount of grain particles (dust) are uniformly dispersed. $\alpha_{\text{ext}}(\lambda)$ may
272 thus be written as the product of the grain extinction cross section, $C_{\text{ext}}(\lambda)$, by the f/V ratio,
273 where f is the volume fraction of grain particles in the sample and V is the volume of a single
274 particle (Bohren and Huffman, 1983). We can imagine grain particles to be compressed
275 within the pellet in a homogeneous slab ($f=1$) of thickness $d = \frac{M}{\rho S}$, with M the total grain
276 mass contained in the pellet, ρ the density of the grain material, and S the surface of the
277 pellet, to obtain:

$$278 \quad \alpha_{\text{ext}}(\lambda) = \frac{C_{\text{ext}}(\lambda)}{V} = \frac{3}{4} \frac{Q_{\text{ext}}(\lambda)}{a} \quad (2)$$

279 where $Q_{\text{ext}}(\lambda)$ is the grain extinction efficiency and a the particle radius. The dust density is
280 set at 2.5 g cm^{-3} for all the samples. This value is chosen approximately at the mean of the
281 range of desert dust densities as reported in the literature, i.e. $2.1\text{-}2.75 \text{ g cm}^{-3}$ (e.g., Maring et
282 al. 2000; Winfield, 2000; Iwasaka et al., 2003; Reid et al., 2003; Fratini et al., 2007).

283 In case extinction is dominated by absorption, $Q_{\text{ext}} \sim Q_{\text{abs}}$, as it can be assumed at infrared
284 wavelengths for dust in pellets, we can write explicitly the $Q_{\text{abs}}(\lambda)/a$ ratio as a function of the
285 measured transmittance as:

286

$$\frac{Q_{\text{abs}}(\lambda)}{a} = \frac{4}{3} \frac{\rho S}{M} \ln \left(\frac{1}{T(\lambda)} \right) \quad (3)$$

287 For very small grains ($a \ll \lambda$, i.e. the Rayleigh limit) embedded in a matrix of transparent
 288 material, the ratio between the absorption efficiency and the particle radius can be written
 289 following Mie theory for Rayleigh spherical particles as (Bohren and Huffmann, 1983):

290

$$\frac{Q_{\text{abs}}(\lambda)}{a} = \frac{8\pi}{\lambda} \sqrt{\epsilon_m} \text{Im} \left(\frac{\bar{\epsilon}(\lambda) - 1}{\bar{\epsilon}(\lambda) + 2} \right) \quad (4).$$

291 $\epsilon_m = (n_{0,m})^2$ is the real dielectric function of the matrix, with $n_{0,m}$ the real component of the
 292 KBr refractive index, and $\bar{\epsilon}(\lambda)$ the dielectric function of the grain material relative to the
 293 matrix. The value of $(n_{0,m})$ for KBr has been set at 1.54, constant in the considered infrared
 294 spectral range, as also reported in Orofino et al. (1998), and thus $\epsilon_m = 2.37$. The verification of
 295 the Rayleigh limit $a \ll \lambda$ has been tested for our dust samples using co-located measurements
 296 of the particle number size distribution (Grimm data shown in Fig. 1 and discussed in the
 297 next sections). At the wavelengths of 10 and 20 μm , the condition $a/\lambda < 0.1$, which can be
 298 considered satisfactory to verify the Rayleigh limit, is fulfilled on average by the 94 and 98%
 299 of particles (in number). Moreover, in our formulation (Eq. (4)) we assume dust particles to
 300 have a spherical shape, and thus to be described by the Mie theory. Taking into account
 301 particles non-sphericity would require a much more complex retrieval scheme. We have
 302 decided to neglect this effect at this stage, thus maintaining retrieval conditions which are
 303 similar to those of previous literature studies on the dust refractive index.

304 The dielectric function in Eq. (4) may be written using the Clausius-Mossotti relation as the
 305 sum of N Lorentzian harmonic oscillators:

306

$$\frac{\bar{\epsilon}(\omega) - 1}{\bar{\epsilon}(\omega) + 2} = \frac{\bar{\epsilon}_v(\omega) - 1}{\bar{\epsilon}_v(\omega) + 2} + \left[\sum_{j=1}^N \frac{F_j}{\omega_j^2 - \omega^2 - i\gamma_j \omega} \right] \quad (5)$$

307 where ω is the angular frequency of radiation ($\omega = 2\pi c/\lambda$, [s^{-1}]), c is the velocity of light in
 308 vacuum, and $\bar{\epsilon}_v$ is the real dielectric function of the grain material relative to the matrix in
 309 the limit of high frequencies, i.e. at visible wavelengths, $\bar{\epsilon}_v = \left(\frac{\epsilon_g}{\epsilon_m} \right)_{\text{vis}}$ with $\epsilon_g = (n_{0,g})_{\text{vis}}^2$ and

310 $\epsilon_m = (n_{0,m})_{\text{vis}}^2$, square of the real components of the refractive index at visible wavelengths

311 for the grain material and the matrix. $(n_{0,m})_{vis}$, and $(n_{0,g})_{vis}$ have been set at 1.57, and 1.53,
 312 respectively, as the mean of the values reported in literature for KBr (e.g. Orofino et al.,
 313 1998) and African dust (Osborne et al., 2008; Petzold et al., 2009; McConnell et al., 2010;
 314 Klaver et al., 2011). Our choice of 1.53 is also in agreement with the values reported by most
 315 of past literature studies on the dust infrared refractive index (see data shown in Fig. 7). (ω_j ,
 316 γ_j , F_j) are the three fundamental parameters characterizing the j -th oscillator, and in particular
 317 ω_j is the eigenfrequency, γ_j is the damping factor, and F_j is a quantity related to the plasma
 318 frequency strength, $\omega_{p,j}$, and the oscillator strength, f_j , through the relation $F_j = \frac{1}{3} f_j \omega_{p,j}^2$. By
 319 combining Eq. (4) and (5), we have:

$$320 \quad \frac{Q_{abs}(\omega)}{a} = \frac{4\omega}{c} \sqrt{\epsilon_m} \left[\sum_{j=1}^N \frac{F_j \gamma_j \omega}{(\omega_j^2 - \omega^2)^2 + \gamma_j^2 \omega^2} \right] \quad (6)$$

321 Starting from the transmission measurements and by applying Eq. (3) an experimental
 322 estimation of the ratio $Q_{abs}(\omega)/a$ can be obtained. A non-linear fit procedure is then applied to
 323 the experimental $Q_{abs}(\omega)/a$ spectrum to determine the $3N$ values of the oscillator parameters
 324 (ω_j , γ_j , F_j) in Eq. (6). Once estimated, the $3N$ parameters are used to calculate the dielectric
 325 function of the grain material relative to the matrix, $\bar{\epsilon}(\lambda)$, by applying Eq. (5). The absolute
 326 dielectric function of the grain material $\epsilon_g(\lambda)$ is then estimated by multiplying $\bar{\epsilon}(\lambda)$ by ϵ_m .
 327 Finally, the spectral real, $n_g(\lambda)$, and imaginary, $k_g(\lambda)$, parts of the grain material complex
 328 refractive index can be determined using the following equations:

$$329 \quad n_g = \left(\frac{1}{2} \left[\sqrt{(\epsilon_g')^2 + (\epsilon_g'')^2} + \epsilon_g' \right] \right)^{1/2} \quad k_g = \left(\frac{1}{2} \left[\sqrt{(\epsilon_g')^2 + (\epsilon_g'')^2} - \epsilon_g' \right] \right)^{1/2} \quad (7)$$

330 The real and imaginary parts of both the dielectric function and refractive index are not
 331 independent quantities. They are related through the Kramers-Kronig relations, which for the
 332 refractive index can be written as:

$$333 \quad n_g(\omega) - 1 = \frac{2}{\pi} P \int_0^\infty \frac{\Omega \cdot k(\Omega)}{\Omega^2 - \omega^2} \cdot d\Omega \quad k_g(\omega) = -\frac{2\omega}{\pi} P \int_0^\infty \frac{n(\Omega)}{\Omega^2 - \omega^2} \cdot d\Omega \quad (8)$$

334 where P is the Cauchy Principal value of the integral. It should be noticed that the retrieval
 335 method based on the Lorentzian dispersion theory used here allows to obtain $(\epsilon_g', \epsilon_g'')$ and
 336 (n_g, k_g) couples which automatically satisfy the Kramers-Kronig relations.

337

338 **2.2 Dust mineralogical composition**

339 Different techniques have been combined to yield the most complete characterization of the
340 composition of mineral dust, including: (i) Wavelength Dispersive X-Ray Fluorescence
341 (WD-XRF, Panalytical PW-2404 spectrometer) to determine the dust elemental composition
342 (Na, Mg, Al, Si, P, K, Ca, Ti, Fe); (ii) X-Ray Diffraction (XRD, Siemens D500
343 diffractometer) to estimate the particles' mineralogical composition in terms of clays
344 (kaolinite, illite, smectite, chlorite), quartz, Ca-rich species (calcite, dolomite, gypsum), and
345 feldspars (orthose, albite); (iii) the CBD-method (Lafon et al., 2004) to determine the dust
346 iron oxide content; (iv) the X-ray Absorption Near Edge Structure (XANES) and Extended
347 X-ray Absorption Fine Structure (EXAFS) to retrieve the iron speciation between hematite
348 and goethite. The details of the experimental protocols and data treatment for the different
349 techniques are extensively discussed in Caquineau et al. (1997 and 2002), Lafon et al. (2004),
350 Klaver et al. (2011), and Formenti et al. (2008; 2014). The full set of mentioned analyses has
351 been carried out on the SOP0-47, SOP1-8, and SOP1-17 samples. Instead, for the N32 and
352 N93 samples only XRD measurements have been possible.

353 Starting from these measurements, the dust mineralogical composition for the different
354 samples has been estimated through the procedure described in Appendix B.

355

356 **2.3 Dust particle size distributions**

357 The particle number size distribution between 0.3 and 20 μm on 15 size channels was
358 measured at the two sampling sites by means of a Grimm OPC (Grimm Inc., model 1.108)
359 (Heim et al., 2008) operated at 1-min (Tamanrasset) and 5-min (Banizoumbou) time
360 resolution. The Grimm OPC was factory calibrated with monodisperse polystyrene sphere
361 latex (PSL) whose complex refractive index at the instrument operating wavelength (780 nm)
362 is 1.59-0i. We have corrected the measured sphere-equivalent optical diameter in a sphere-
363 equivalent geometrical diameter by taking into account the complex refractive index of the
364 sampled aerosol (Liu and Daum, 2000). The optical-to-geometric diameter conversion has
365 been done by recalculating the calibration curve considering the refractive index of dust
366 aerosol. Optical calculations have been performed using Mie theory for spherical particles.
367 The complex refractive index was set at 1.53-0.002i, in the range of values available in the
368 literature for Saharan dust (e.g., Osborne et al., 2008; Petzold et al., 2009). After refractive

369 index correction the diameter measurements range for the Grimm 1.108 became 0.38-28.9
370 μm .

371 The average of the size distribution data measured in correspondence of each of the five dust
372 filter samplings has been calculated. Continuous Grimm data were available for the three
373 Banizoumbou SOPs dust events, whereas Tamanrasset measurements were acquired only at
374 the end of the dust episode for N32 (26 July 2006 from 10:00 to 14:17) and at the beginning
375 for N93 (5 October 2006 between 01:00 and 8:07).

376

377 **3. Physico-chemical properties of the selected dust cases**

378 Figure 1 shows the normalised number and volume size distributions obtained for the five
379 different dust events considered in this study. All size distributions are characterised by a
380 multimodal structure with five main modes, in volume centred at about <0.6 , 1, 2.5, 5, and 12
381 μm diameters. Because of the lower size cut of the Grimm OPC at $0.3 \mu\text{m}$, the lower tail of
382 the first mode at diameter $<0.6 \mu\text{m}$ is not very well defined. N32 and N93 distributions show
383 also an additional defined mode, centred at $\sim 25 \mu\text{m}$, not present in the SOPs cases. This
384 additional mode is possibly associated to resuspension of particles very locally at the
385 Tamanrasset site during the dust events. In terms of number distributions, the samples show a
386 similar particle content in the whole size range, with the exception of SOP1-8, which is richer
387 in coarse particles (diameter $>5 \mu\text{m}$), and N93, which presents a lower particle content in the
388 whole diameter range $\sim 0.8-25 \mu\text{m}$. For N93, this is likely due to the fact that Grimm has
389 measured at the very early stage of the dust event, thus before the maximum of the
390 atmospheric dust load. In order to model the behaviour of the size distribution data,
391 multimodal lognormal fits have been performed, and the fitting curves obtained are also
392 shown in Fig. 1. Seven lognormal modes have been necessary to fit the experimental curves.
393 The mean of the 5 lognormal fitting curves obtained considering (mean_A) or discarding
394 (mean_B) the N32 and N93 mode at $25 \mu\text{m}$ has been calculated, and data are also plotted in
395 Fig.1.

396 The mineralogical composition obtained for the five dust samples is reported in Table 2 and
397 summarized in what follows: (i) SOP0-47 and N32 are originated in the same source areas in
398 North - Northwestern Niger, so they are essentially characterized by the same mineralogical
399 composition with $\sim 89-90\%$ of clays, 6% of quartz, and 4% of iron oxides. The only
400 significant difference between the two is the clays partitioning, with only kaolinite and illite

401 detected in SOP0-47, and also smectite identified as a major clay component in N32; (ii) even
402 if sampled during a Sahelian erosion event, SOP1-17 presents a mineralogy very similar to
403 that of SOP0-47 and N32. This may be explained considering that SOP1-17 particles has
404 been collected more than 3 hours after the main erosion event had occurred, so likely after the
405 dust plume has been deprived of its component of larger particles, rich in quartz and
406 feldspars, due to the rapid gravitational settling process (Pye, 1987). This is also consistent
407 with the measured size distribution for this sample. For SOP1-17, the only case for which
408 iron speciation is available, goethite is observed to dominate over hematite (80% vs 20% of
409 the iron oxide content); (iii) SOP1-8, sampled in correspondence of a strong Sahelian local
410 erosion event, differs from all the other samples because of its low amount of clays (52%),
411 mainly kaolinite and illite, and enrichment in quartz (40%) and feldspars (3%). The high
412 quartz content also explains the larger fraction of particles, especially of diameter larger than
413 ~10 μm , which account for ~60% of the particle volume size distribution, observed for this
414 sample; (iii) N93 is characterized by a lower content of clays (67%), mainly kaolinite and
415 smectite, together with larger amounts of quartz (17%) and Ca-rich species (11% of calcite
416 and gypsum), the latter in particular indicative of Northwestern Sahara source areas.

417

418 4. Results

419 4.1 Dust infrared absorption spectra

420 The absorbance spectra ($A = \log_{10}(1/T)$, with T the transmittance) measured in the spectral
421 range 2.5-25 μm for the five different dust samples are shown in Fig. 2. The uncertainty on
422 the measured spectra is less than 3% and has been estimated as the 3σ variability of the signal
423 in the regions of no dust absorption ($A < 0.01$). This uncertainty takes into account for the
424 variability of the noise and the offset components of the measured signal.

425 The main features of the different spectra essentially follow the signatures of clay species
426 (kaolinite, illite, smectite; see Fig. 3 as a reference for single mineral features and Table 3 for
427 identified band positions and their assignments). The dust largest absorption is observed in
428 the window region 8-12 μm (maximum of A from 0.08 to 0.21) and at wavelengths larger
429 than ~17 μm (maximum of A from 0.04 to 0.10), therefore where the strongest absorption
430 bands of clays are found. Coincident or superimposing bands for the different clay species are
431 present at ~9.0, 9.7, 9.9, 18.8, 19.3, 21.4, and 23.1 μm (bands peak wavelengths), while an
432 additional single band mainly associated to kaolinite is identified in the 10.4-11.2 μm spectral

433 region. Absorption by quartz in the atmospheric 8-12 μm window region (single band at ~9.2
434 μm) and above 17 μm (two bands centred at ~20 and 22 μm) appears to be masked by the
435 clay signals, while a more clear signature emerges at ~12-13 μm . This is the case for the
436 quartz-rich SOP1-8 sample which shows an enhanced absorption over this band compared to
437 the other dust cases. The calculated ratio of the quartz band peak intensity (at ~12.5 μm)
438 between SOP1-8 and the other samples varies between a minimum of 1.32-1.36 for SOP1-17
439 and N93 to a maximum of 1.45-1.56 for SOP0-47 and N32, thus indicating the contribution
440 of quartz in SOP1-8 to determine about 30-50% increase of the absorption in this band.

441 As for the quartz, also the spectral signatures of the other minerals, e.g. Ca-rich species, are
442 apparent only when the absorption of clays becomes very low. This is the case of sample N93
443 for which it is possible to detect the signal of calcite at ~7 and ~11.4 μm , and also of gypsum,
444 whose band between 8.2 and 9.2 μm appears to combine with the clays and quartz bands
445 determining a broadening of the N93 spectrum in this part of the window spectrum. A small
446 signature is also observed for all the different samples between 14 and 16 μm , possibly
447 associated to the combined effect of Ca-rich minerals and iron oxides absorbing in this
448 spectral interval (calcite, gypsum, hematite, goethite). Strongest signatures of iron oxides,
449 which mainly occur at wavelengths larger than 15 μm (two large bands centred at ~19 and
450 23 μm for hematite, and one at ~18 μm for goethite), are instead very difficult to detect due
451 to their superposition with clay bands.

452 Almost negligible differences in terms of the position of the absorption bands are observed
453 for the different samples. Conversely, a marked sample-to-sample variability of the amplitude
454 of the band peaks is noticed. In general, the lowest absorbance is observed for SOP1-8 while
455 highest values are obtained for N32 and N93. This is likely linked to the clay content and its
456 speciation, as well as dust size distribution, for the different dust cases. The weaker
457 absorption observed for SOP1-8, for instance, can be associated to the lowest illite and
458 kaolinite content measured for this sample, thus reducing the clay minerals absorption
459 features. The largest absorption of N32 and N93 may be instead related, at least as first
460 assumption, to the presence of smectite as a dominant clay species together with kaolinite.
461 Major absorption bands of smectite are, in fact, coincident and comparable or even stronger
462 in intensity to those of kaolinite, so the combined effect of the two clays results in an
463 enhancement of the absorption at these wavelengths. There is also another consideration to
464 possibly explain the larger absorption obtained for the N32 and N93 samples. As already
465 pointed out in Sect. 3, the two Tamanrasset samples present in their size distribution a

466 defined mode of larger particles, more efficient in interacting with infrared radiation,
467 compared to the Banizoumbou samples. This means that, even with a similar mineralogical
468 composition of dust between the two sites, we have to expect larger absorption for
469 Tamanrasset dust due to the differences in the size distribution. This assumption can be
470 tested, for instance, by considering the peak value of kaolinite band at $\sim 10.9 \mu\text{m}$, for which
471 we obtain slightly larger intensities for N32 and N93 samples (0.046 and 0.05, respectively)
472 compared to those of the SOPs samples (0.043 for SOP0-47 and 0.033 for SOP1-8 and
473 SOP1-17), which we know to have a similar or rather larger content of kaolinite. The role of
474 the size distribution possibly allows also to explain the fact that sample N93, which has a
475 global smaller content of clays but a larger fraction of coarse particles, presents an absorption
476 which in intensity is comparable to that of the clay richer N32. The fact of observing
477 differences in the absorption spectra which are coherent with the variability of the size
478 distribution measured for the different samples indicates that the main features of dust size
479 have little changed during sample manipulations and pellet production.

480 Few narrow peaks are also observed at $\sim 2.7 \mu\text{m}$ for all the samples, at $\sim 4.2 \mu\text{m}$ for SOP0-47 and
481 SOP1-17, and at $\sim 7.2 \mu\text{m}$ for SOP0-47, SOP1-8, and SOP1-17. The peaks at 4.2 and $7.2 \mu\text{m}$
482 are very likely due to CO_2 and organic matter, respectively, which have contaminated the
483 samples after dust-KBr pellet production. The intensity of these narrow peaks appears, in
484 fact, to be proportional to the absorption band of H_2O observed between ~ 2.7 and $4 \mu\text{m}$ for
485 all the samples (not shown in the spectra of Fig. 2 because removed through baseline
486 correction), which in turn is associated to the KBr water absorption occurred meanwhile
487 spectroscopic manipulations. Absorption by carbonate species (i.e., calcite) may also partly
488 contribute to the $7.2 \mu\text{m}$ band. The signal measured at $2.7 \mu\text{m}$ is instead mainly related to
489 clays (kaolinite and illite) (Saikia and Parthasarathy, 2010). These narrow peaks have been
490 thus taken into account for successive analyses.

491

492 **4.2 Dust infrared complex refractive index**

493 Starting from the measured transmittance spectra, the $Q_{\text{abs}}(\lambda)/a$ ratio has been calculated by
494 applying Eq. (3). The uncertainty on the calculated $Q_{\text{abs}}(\lambda)/a$, taking into account the
495 uncertainties on the measured spectra ($< 3\%$) and the estimated pellet dust content ($< 7\%$),
496 varies between a minimum of 2.4% for N32 to a maximum of 6.4% for SOP1-8. As discussed
497 in Sect. 2.1, a non-linear fit procedure has been applied to the experimental $Q_{\text{abs}}(\lambda)/a$ to

498 obtain the values of the 3N parameters necessary to estimate the real and imaginary parts of
499 the dust refractive index. The fitting procedure has been performed using the Levenberg-
500 Marquardt technique (e.g., Pujol, 2007). Reasonable guesses for the oscillator parameters are
501 manually entered as inputs, then the fitting routine returns optimized parameters. The initial
502 number and position of oscillators is set to be equal to that of the absorption bands present in
503 the experimental $Q_{\text{abs}}(\lambda)/a$ spectrum. Additional oscillators may be subsequently added in
504 order to improve the results of the best fit procedure. To guarantee a successful analysis,
505 however, the number of fitting oscillators should remain limited; furthermore, the obtained
506 3N oscillator parameters must all have positive values (Spitzer and Kleinman, 1961; Roush et
507 al., 1991). The experimental $Q_{\text{abs}}(\lambda)/a$ spectra together with the theoretical curves obtained
508 from the nonlinear fitting procedure are shown in Fig. 4. The number of oscillators used for
509 each fit, also reported in the plot, is between 22 and 29. Residuals (R) between the
510 experimental and the fitted $Q_{\text{abs}}(\lambda)/a$ and normalized by the measurement error have been
511 calculated to verify the goodness of the results. An example is shown in Fig. 5, where the
512 spectral R obtained for two of the five analysed dust samples (SOP1-8 and N93) are plotted.
513 It indicates that the $Q_{\text{abs}}(\lambda)/a$ spectra are fitted within their estimated uncertainty ($|R| \leq 1$)
514 approximately in the entire wavelength range with significant absorbance ($A > 0.01$).
515 Discrepancies between the experimental and the fitted curves ($|R| \leq 10$) are obtained for $\lambda < 6.7$
516 μm and in few narrowbands between 12 and 17 μm , thereby in spectral regions where dust
517 absorption is close to zero. The set of 3N parameters estimated from the $Q_{\text{abs}}(\lambda)/a$ fits have
518 been used to calculate, by applying Eqs. (5) and (7), the real and the imaginary parts of the
519 refractive index.

520 A sensitivity analysis was carried out in order to assign an uncertainty to the retrieved values
521 of n and k , whose determination is based on a minimization procedure. The sensitivity
522 analysis is aimed at assessing how the uncertainties on the measured $Q_{\text{abs}}(\lambda)/a$ affect the
523 retrieved parameters. To this purpose, the values of n and k are also obtained by using as
524 input the observed $Q_{\text{abs}}(\lambda)/a \pm$ one standard deviation on their measurement. The deviations
525 of the values of n and k retrieved in the sensitivity study with respect to those obtained in the
526 first inversion are assumed to correspond to the one standard deviation uncertainty. The
527 results show the uncertainty is small (<1.5%, averaged over the whole spectral range) for the
528 real part of the refractive index, while more significant (<25%) for the imaginary part.
529 Another source of uncertainty for n and k , which we do not quantify in this study, is also

530 associated to the choice of the $(n_{0,m})_{vis}$ value in Eqs.(5)-(7), here set at 1.53 in agreement with
531 past literature studies (Volz, 1973; Carlson and Benjamin, 1980; Longtin et al., 1988).

532 The real and the imaginary parts of the refractive index obtained for the five dust samples
533 considered in this study are shown in Fig. 6. As expected, the retrieved n and k reproduce
534 well the features detected in the absorbance spectra, both in terms of spectral signature and
535 relative intensities between the different samples. Evident is the contribution of clays,
536 especially in the 8-12 μm and 17-25 μm spectral intervals where multiple bands, reproducing
537 the absorption due to kaolinite, illite, and smectite, are observed. The sharp transition from
538 low absorption outside these spectral ranges to the maxima absorption within them,
539 determines the largest variations of the refractive index. In the 8-12 μm window, the
540 imaginary part rapidly increases from ≤ 0.001 to peak values of 0.3- 0.85, while the real part
541 ranges between 1.1 and 2.0. Above 17 μm , k peaks at 0.45-1.0, and n varies between 1.2 and
542 2.7. As for the absorbance, refractive index data display a very weak quartz signature, with
543 the only exception of the 12-13 μm band, where the absorption of quartz induces an increase
544 of k to values of ~ 0.09 for SOP1-8 and < 0.06 for the other samples. The contribution of
545 calcite to the refractive index of N93 is marked at $\sim 7 \mu\text{m}$ ($k \sim 0.07$), while it is almost
546 indistinguishable at $\sim 11.4 \mu\text{m}$. Also, a refractive index comparable to that of quartz and
547 calcite ($k \sim 0.06-0.08$) is observed at 14-16 μm due to the combination of calcite, gypsum, and
548 iron oxides signatures.

549 A small red shift of less than 0.3 μm (or 10 cm^{-1}) is observed in correspondence of the
550 different refractive index peaks compared to the experimental absorption spectra. This is
551 possibly associated to the fact of using Mie theory to reproduce dust absorption in our
552 retrieval algorithm. Our 10 cm^{-1} shift is however smaller compared to the $25-40 \text{ cm}^{-1}$ Mie
553 induced shift reported by several authors investigating the extinction spectra of several clay
554 and non-clay dust constituent minerals (Hudson et al., 2008a and 2008b; Laskina et al. 2012).
555 This suggests the effect of shifting due to the use of Mie theory to be partly mitigated when
556 considering the extinction spectra of dust particles instead of single minerals.

557 Our results show the dust refractive index to significantly vary in magnitude for the five
558 analysed samples. For instance, within main clay absorption bands we obtain for N32 and
559 N93 values of k which are 2-3 times larger compared to SOP1-8. Differences up to 30-40%
560 are also observed for the real part in the considered cases. As discussed in Sect. 4.1, this
561 variability is linked to the variability of mineralogical composition and size distribution

562 observed for the different dust events. In conclusion, these results, despite obtained
563 considering aerosols from a limited number of sources from Western Africa, appear rather
564 significant as they clearly put in evidence the large sensitivity of the refractive index to the
565 physico-chemical properties of dust particles.

566

567 **4.3 Comparison with literature data and the OPAC database**

568 The results of our analysis have been compared with other studies providing direct estimates
569 (pellet spectroscopy data on dust collected at different sites, i.e. Germany, Barbados, Niger;
570 Volz, 1972, and 1973; Fouquart et al., 1987), and mineralogy-based calculations (Longtin et
571 al., 1988) of the dust infrared refractive index, as well as syntheses of available literature data
572 (Carlson and Benjamin, 1980; Sokolik et al., 1993). These studies have been selected as they
573 serve as the main basis for models for aerosol optical properties (e.g., Toon and Pollack,
574 1976; Shettle and Fenn, 1976 and 1979; WMO, 1986; D'Almeida, 1991) and global aerosol
575 databases, such as OPAC and GADS, all extensively used in a wide variety of radiative and
576 climatological studies. Besides, the OPAC aerosol database plays a very important role in
577 satellite remote sensing as it is the most used reference for dust properties in the retrieval
578 algorithms of several sensors measuring in the thermal infrared (MODIS, SEVIRI, AVHRR,
579 HIRS, AIRS, IASI) (see Table 1 in Klüser et al., 2012). Owing to its widespread utilisation
580 and relevance for atmospheric application, the complex refractive index of the desert aerosol
581 model from the OPAC database is also considered for comparison with our results.

582 The results of the comparison are shown in Fig.7. For both the real and the imaginary parts,
583 our estimates of the dust refractive index fall, over the whole considered spectrum, in the
584 range of variability reported in literature data. For the imaginary part, a similar spectral
585 behaviour is observed in the 8-12 μm window region between our data and the different
586 literature curves, with the only exception of Longtin et al. (1988) due to the large contribution
587 of quartz in their calculations. The spectral signatures from the different clay species appear
588 smoothed in the curves taken from literature, mainly because of the rather coarse spectral
589 resolution of these datasets. Only a major single peak between 9 and 10 μm is observed,
590 compared to our data where multiple clay peaks are detected in the 8-12 μm spectral interval.
591 The majority of the different datasets presents the signature of calcite at $\sim 7 \mu\text{m}$ in the k
592 spectrum, as also observed in our data for the N93 sample. Above 11-12 μm , the imaginary
593 part of the refractive index obtained in this study is lower in magnitude compared to most of

594 literature data at nearly all spectral bands. For the real part of the refractive index, a
595 comparable spectral variability is obtained between our data and the different literature
596 datasets in the 2.5-17 μm spectral range, also if a significant weaker variation is observed for
597 our results in the 8-12 μm window. The best agreement, also in terms of measured intensity,
598 is found with the real part by Volz (1972) in the whole 8-25 μm interval. For literature data,
599 and Longtin et al. (1988) in particular, a stronger contribution of quartz is observed in both
600 the real and the imaginary spectra, with strong peaks detected at \sim 9.2, 12.5, 20 and 22 μm .
601 Furthermore, above 17 μm the different datasets, with the only exception of Fouquart et al.
602 (1987) and in part Volz (1973), appear to mostly neglect the signatures of clays, which
603 instead are observed to dominate our n and k experimental curves.

604 For both the real and the imaginary parts, the ensemble of literature data and our estimates
605 are observed to span a relative large interval of values. This variability is related, as a first
606 hypothesis, to the fact that the different studies refer to dust from diverse source regions as
607 well as to different stages of their atmospheric lifetime, thus to particles characterized by a
608 different composition and size distribution, so optical properties. A large variability of the
609 dust infrared refractive index has been also documented by Patterson et al. (1981) and Otto et
610 al. (2007), who compiled literature data from additional studies. For instance, for the
611 imaginary part they reported a range of values spanning the interval 0.02-1.0 at 8-12 μm ,
612 comparable to that in Fig. 8. Thus, the comparison between our results and literature data
613 confirms the large variability of the dust infrared complex refractive index as a function of
614 the physico-chemical properties of the particles.

615 As discussed by Sokolik et al. (1993), however, differences between the various datasets
616 might be associated not only to the specific physico-chemical state of the particles, but also to
617 uncertainties due to the different methods used to estimate the dust refractive index. This is,
618 for instance, the case when comparing our data with those by Volz (1972) and (1973). In
619 these studies the real and imaginary parts of the dust refractive index were derived by two
620 different measurements: the imaginary part using transmission measurements and the real
621 part using reflectance measurements, both with the standard pellet technique. For the
622 imaginary part, the transmission spectra inversion was performed by applying a method
623 which is mostly consistent with our approach, as discussed in Sect. 2.1, and this also explains
624 the good comparison with our data for k . For the real part they inversed the reflectance
625 spectra by combining the specular reflectance law and the previous estimated imaginary part
626 of the refractive index. We found, however, that by following this procedure they obtained

627 real and imaginary parts of the refractive index which do not verify the Kramers-Kronig
628 relationship, and this explains why there is a larger disagreement with our results especially
629 in the 8-12 μm window for n . Similar considerations are valid also for Carlson and Benjamin
630 (1980) and OPAC data. This also implies that caution has to be used when making use of
631 these refractive index data as, from a theoretical point of view, they are incorrect.

632

633 **5. Infrared intensive optical properties of mineral dust: variability and implications**

634 **5.1 Sensitivity to refractive index and size distribution**

635 Intensive optical properties relevant to radiative transfer (mass extinction efficiency, k_{ext} ,
636 m^2g^{-1} ; single scattering albedo, ω ; asymmetry factor, g), have been calculated for the five
637 analysed dust samples based on their estimated complex refractive index and measured
638 particle size distribution.

639 Two sets of k_{ext} , ω , and g have been computed: (i) at first, calculations have been performed
640 by considering for the different samples their own complex refractive index, while fixing a
641 unique size distribution for all the cases (i.e., the mean_B average size distribution shown in
642 Fig.1). This permits to focus exclusively on the effect of refractive index variability on the
643 estimated properties; (ii) as a second approach, k_{ext} , ω , and g have been calculated by taking
644 into account for the own dust sample complex refractive index and size distribution. In this
645 case, the combined effect of refractive index and size distribution variability will emerge
646 from the results. In this study, we have decided to neglect the effect of particle shape (e.g.,
647 Kalashnikova and Sokolik, 2002; Nousiainen, 2009), and dust optical calculations have been
648 performed using Mie theory for spherical particles. The ensemble of calculated dust optical
649 properties is reported in Fig. 8. By comparison, also the spectral optical properties obtained
650 using the OPAC refractive index, calculated considering the mean_B size distribution, are
651 shown in the plot.

652 We consider at first data obtained for the fixed dust size distribution (Fig. 8a). Calculated
653 optical properties, k_{ext} and ω in particular, follow the spectral signature and variability of the
654 complex refractive index, with the strongest absorption observed in the window region and at
655 wavelengths $>17 \mu\text{m}$. k_{ext} and ω vary in the range $\sim 0.05-0.25$ and $\sim 0.25-1.0$, respectively.
656 The asymmetry factor is observed to decrease approximately linearly with λ for all the
657 samples, with values ranging from a maximum of ~ 0.75 at $2.5 \mu\text{m}$ to a minimum of 0.25 at
658 $25 \mu\text{m}$. Moderate differences are obtained between the different samples for k_{ext} and g , while

659 larger variations are observed for ω , especially below 10 μm and in the range 12-23 μm . In
660 comparison to our data, the calculation based on the OPAC refractive index appear to
661 overestimate dust extinction (up to $0.1 \text{ m}^2 \text{ g}^{-1}$ increase), especially at 9-10 μm , mainly due to
662 the stronger contribution of scattering for the OPAC real refractive index, and at 12-14 μm , in
663 correspondence of the quartz band. Absorption from OPAC is considerably larger than our
664 estimates at the 2.5-8 μm and 11-17 μm spectral ranges, with differences in ω reaching up to
665 0.6 at several bands. An underestimation of the dust absorption is observed in the window
666 region between 9 and 10 μm , with differences in ω up to 0.15. When looking at the
667 asymmetry factor, OPAC calculations appear quite in agreement with our results in
668 reproducing the magnitude and the spectral decrease of g .

669 As expected, the differences between the different samples, and also between our samples
670 and OPAC, considerably increase when the own size distribution for each case is taken into
671 account (Fig. 8b). k_{ext} , ω , and g vary in this case in the range ~ 0.05 - 0.35 , ~ 0.25 - 1.0 , and
672 ~ 0.05 - 0.75 , respectively. The largest differences, compared to the results of Fig. 9a, are
673 obtained for N93, due to the combination of a relatively high refractive index and a strong
674 fraction of coarse particles for this sample. Significant differences can be also observed for
675 SOP1-17, especially at $\sim 10 \mu\text{m}$ and for wavelengths $< 6 \mu\text{m}$, mainly due to the presence of a
676 dominant particle mode centred at 5 μm . SOP1-8, although very rich in coarse particles,
677 presents, in a wide spectral range, the lowest k_{ext} and highest ω (i.e., less absorption), and this
678 is caused by the very low values of the refractive index measured for this sample compared to
679 the other dust cases. However, for SOP1-8 sample the effect of having a dominant mode of
680 coarse particles strongly influences g , for which the largest values are obtained.

681 The comparison of our results with those obtained in other studies is very difficult due to the
682 large variety of refractive index and size distribution data used in the literature. McConnell et
683 al. (2010), for instance, have estimated intensive optical properties in the spectral range 0.2-
684 10 μm for Western Saharan dust aerosols based on internal and external mineralogy-based
685 calculations of the refractive index and aircraft in situ measurements of the particle size
686 distributions. Our results (Fig. 8a) for both k_{ext} and g appear in reasonable agreement (less
687 than about 0.05 absolute difference in mean) with the estimates by McConnell et al. (2010),
688 while lower values (up to 0.2 absolute value difference) are obtained in our study for the
689 single scattering albedo in the window region. In another study, Hansell et al. (2011) have
690 analysed the variability of k_{ext} as a function of the physico-chemical properties of dust,
691 therefore by testing a large number of models for refractive index and particle size

692 distribution. Their results span a relatively extended interval, with k_{ext} in the 8-12.5 μm
693 spectral region varying between about 0 and $1.2 \text{ m}^2 \text{ g}^{-1}$. Our results fall in the range of
694 variability reported in that study. Hansell et al. (2011) have also shown that the differences in
695 k_{ext} due to the variability of the refractive index and size may significantly amplify when the
696 effect of the shape of particles is considered in the optical calculations. This aspect deserves
697 to be accounted for in future investigations.

698

699 **5.2 Implications for satellite remote sensing**

700 The possible impact of the variability of the dust infrared optical properties on the bands used
701 for satellite retrievals has been investigated. The main information used by the different
702 satellite inversion algorithms to estimate various dust parameters, such as optical depth at 10
703 μm , altitude, or effective radius, is the priori estimate of its spectral infrared optical depth
704 (Pierangelo et al., 2004; Klüser et al., 2011 and 2012). Therefore, to test the satellite
705 sensitivity to dust properties we have focused on the differences between our estimates of k_{ext}
706 and those based on the OPAC model in the window spectral region. The variability of the
707 spectral mass extinction coefficient is, in fact, proportional to the variability of the aerosols
708 spectral optical depth. The calculated k_{ext} in the 8-12.5 μm range is shown in Fig. 9, where
709 also the main bands for dust retrieval in the thermal infrared from the AIRS and IASI
710 satellites are reported. In most of cases, with the exception of the channels at $\sim 8 \mu\text{m}$, the
711 OPAC k_{ext} is observed to fall approximately at the mean of the ensemble of values estimated
712 in this study. A disagreement up to $0.1 \text{ m}^2 \text{ g}^{-1}$, corresponding to 50-100% of the OPAC k_{ext}
713 absolute value, is observed with respect to the minimum and maximum of k_{ext} for our
714 samples in correspondence of the different AIRS and IASI bands. Considerable differences in
715 term of spectral variation are also obtained between the OPAC and our experimental k_{ext} ,
716 especially in the 8.5-10 and 11-12.5 μm regions. The results of this simple comparison
717 suggest that the fact of not taking into account the variability of dust properties, i.e. using the
718 OPAC model in satellite inversion algorithms, is expected to possibly induce a significant
719 source of uncertainty on the dust retrievals.

720 Dust absorption also affects the satellite retrieval of key land and atmospheric parameters. In
721 Fig. 9, for instance, we also report the two MODIS thermal infrared broadband channels, the
722 31 and 32 centred at 11 and 12 μm , used to estimate the Sea Surface Temperature (SST). The
723 retrieval scheme for SST uses the estimated brightness temperature at the two channels (BT_{11}

724 and BT_{12}), as well as their calculated difference ($BT_{11}-BT_{12}$). The absolute value and spectral
725 variations of k_{ext} affect both quantities. The dust effect on the retrieval of BT_{11} and BT_{12} has
726 been reported by several authors to be one of the causes for the observed bias between
727 satellite derived SST and surface measurements (May et al., 1992; Chan and Gao, 2005;
728 Merchant et al., 2006). The OPAC model is not able to reproduce the variability of the k_{ext} ,
729 both in terms of absolute intensity and spectral changes, therefore contributing to the
730 uncertainties in SST estimations. For example, the integrated area of k_{ext} over the 11 and 12
731 μm MODIS bands is 0.089 and 0.087 for OPAC, compared to 0.123 and 0.110 for the
732 maxima values of k_{ext} at the two bands (sample N93, green dashed line), and 0.067 and 0.054
733 for the corresponding k_{ext} minima (samples SOP1-8, light-blue dashed line, and N32, blue
734 dashed line). These results indicate that, with respect to our data, OPAC may underestimate,
735 approximately by a factor 2 and an order of magnitude, respectively, the absolute intensity
736 and the spectral variability of the dust signature at the 11 and 12 μm bands, therefore
737 contributing to the uncertainties on SST estimations.

738 All these considerations thus evidence the necessity for a new optical model, to use in place
739 of OPAC, able to provide a better description of the spectral and regional variability of dust
740 properties. The use of this new model would help increasing the accuracy of satellite
741 inversions over regions affected by the presence of dust.

742

743 **5.3 Implications for dust radiative forcing**

744 k_{ext} data can be also used to provide with a first guess approximation of the dust infrared
745 radiative forcing sensitivity to dust properties. To that we have decided to focus on the
746 forcing efficiency (FE, $W m^{-2} \tau^{-1}$) which is the key parameter describing the aerosol radiative
747 effect. FE is defined as the ratio between the radiative forcing, generally calculated over the
748 whole solar or infrared broadband ranges, and the aerosol optical depth, usually taken at
749 visible wavelengths. The calculation of the forcing efficiency with respect to the optical depth
750 at another wavelength λ_1 (FE_{λ_1}) to that in the visible (FE_{vis}), can be performed through the
751 relation:

752
$$FE_{\lambda_1} = FE_{vis} \frac{\tau_{vis}}{\tau_{\lambda_1}} \quad (9).$$

753 The $\frac{\tau_{\text{vis}}}{\tau_{\lambda_1}}$ term is a non linear function of the aerosol size and refractive index, and may
754 strongly vary as a function of the intensity of absorption bands at infrared wavelengths. Here
755 we want to test the changes in the dust infrared FE when this is calculated with respect to the
756 optical depth at 8, 10, and 12 μm . For the dust infrared forcing efficiency, we have taken as a
757 reference the mean of the cloud-free FE_{vis} values reported by Brindley and Russel (2009) at
758 the top of the atmosphere (TOA) for North Africa ($\sim 15 \text{ W m}^{-2} (\tau^{-1})_{0.55\mu\text{m}}$). Calculations of
759 $\text{FE}_{8\mu\text{m}}$, $\text{FE}_{10\mu\text{m}}$, and $\text{FE}_{12\mu\text{m}}$ have been performed for samples SOP0-47, N32, and N93, for
760 which measurements of the optical depth at 0.50 μm , i.e. the τ_{vis} , were available from
761 AERONET data at the stations. The optical depth at 8, 10, and 12 μm for SOP0-47, N32, and
762 N93 has been calculated as the product between k_{ext} (Fig. 9, dashed curves) and the column
763 dust load, DL (g m^{-2}) estimated for each case. DL has been retrieved as the ratio of the
764 measured $\tau_{0.50\mu\text{m}}$ and the $(k_{\text{ext}})_{0.50\mu\text{m}}$, which in turn has been calculated with the Mie theory
765 considering the measured dust size distribution and assuming a particle refractive index at
766 0.50 μm of $1.53 - 0.002i$. The obtained $\tau_{8\mu\text{m}}$, $\tau_{10\mu\text{m}}$, and $\tau_{12\mu\text{m}}$ and associated FE are reported
767 in Table 4. The dust optical depth at infrared wavelengths varies between a minimum of 0.10
768 to a maximum of 0.92, with resultant $\tau_{0.50\mu\text{m}}$ to $\tau_{8\mu\text{m}}$, $\tau_{10\mu\text{m}}$, and $\tau_{12\mu\text{m}}$ ratios between 1.4 and
769 3.6. The calculated $\text{FE}_{8\mu\text{m}}$, $\text{FE}_{10\mu\text{m}}$, and $\text{FE}_{12\mu\text{m}}$ are thus up to more than three times larger than
770 $\text{FE}_{0.50\mu\text{m}}$, with an estimated maximum of $54.0 \text{ W m}^{-2} \tau^{-1}$. The forcing efficiency shows
771 significant variations as a function of the wavelength, as well as an important sensitivity to
772 the variability in the optical properties of dust. Differences of the FE for the three cases are
773 relatively small at 10 μm ($\sim 2-4 \text{ W m}^{-2} \tau^{-1}$, corresponding to 9-18% difference), and increases
774 at 8 and 12 μm (up to $\sim 10-12 \text{ W m}^{-2} \tau^{-1}$, corresponding to about 30% difference). Hence,
775 these results underline the significant role of the optical properties in modulating the infrared
776 radiative impact of dust.

777

778 **6. Conclusions**

779 In this paper we have presented new experimental estimates of the infrared complex
780 refractive index of African mineral dust. The particle refractive index has been derived from
781 laboratory transmission spectra (2.5-25 μm) by applying a retrieval algorithm which
782 combines Mie and Lorentz dispersion theories. Spectroscopy measurements have been
783 performed on five natural dust samples collected at the sites of Banizoumbou (Niger) and

784 Tamanrasset (Algeria) during the AMMA campaign in 2006 and which originated in different
785 Western Saharan and Sahelian source regions. Co-located in situ measurements of the dust
786 size distribution and laboratory analyses of particle mineralogy have been considered
787 together with spectroscopy data in order to relate the spectral features of the refractive index
788 to the physico-chemical properties of the particles. The main results of our study may be
789 summarized as follows:

- 790 1. For all the different samples, the measured dust absorption spectra and estimated complex
791 refractive index are strongly sensitive to the mineralogical composition of the particles.
792 The main features of the different spectra follow the signatures of clay species (kaolinite,
793 illite, smectite), with the largest absorption bands observed in the 8-12 μm and 17-25 μm
794 spectral regions. In the 8-12 μm window, the imaginary part rapidly increases from ≤ 0.001
795 to peak values of 0.3-0.85, while the real part ranges between 1.1 and 2.0. Above 17 μm , k
796 peaks at 0.45-1.0, and n varies between 1.2 and 2.7. Absorption by quartz and other minor
797 minerals, such as Ca-rich species, arises only when the clay signature becomes very low.
798 Absorption by iron oxides is observed to be almost negligible, in contrast with its crucial
799 role at solar wavelengths (Sokolik and Toon, 1999).
- 800 2. Our results show the dust refractive index to significantly vary in magnitude for the five
801 analysed cases. Differences between maxima and minima values within main absorption
802 bands for the different samples may reach 1.0 for n and 0.6 for k, corresponding to ~40%
803 variability for n and changes of a factor 2-3 for k. The variability of n and k is linked to the
804 variability of particle mineralogy, mainly clay amount and speciation, and, to a lesser
805 extent, size distribution, in particular the coarse fraction.
- 806 3. The results of this study have been compared with other direct spectroscopy estimates and
807 indirect calculations of the infrared refractive index available in the literature and
808 corresponding to dust collected both close to their source regions and along their
809 atmospheric transport. The comparison indicates the results of our study and literature data
810 to be comparable in magnitude. However, when related to our results, literature data
811 appear to fail in reproducing the signatures of main minerals, in particular clays and
812 quartz. Furthermore, the real and the imaginary parts of the refractive index from part of
813 literature studies are found not to verify the Kramers-Kronig relations, thus resulting
814 theoretically incorrect. The comparison between our results, from Western Africa, and
815 literature data, from different locations in Europe, Africa, and the Caribbean, nonetheless,

816 confirms the expected large spatio-temporal variability of the infrared refractive index of
817 dust, thus highlighting the necessity for an extended systematic investigation.

818 5. Aerosol intensive optical properties relevant to radiative transfer (k_{ext} , ω , g), have been
819 calculated for the five analysed dust samples based on their estimated complex refractive
820 index and measured particle size distribution. Results indicate a strong sample-to-sample
821 variability for dust infrared optical properties, with k_{ext} , ω , and g varying in the range 0.05-
822 0.35, 0.25-1.0, and 0.05-0.75, respectively, due to the combined changes of both the
823 refractive index and size distribution for the different samples. This observed variability
824 has been tested to possibly have a significant impact on satellite retrievals and dust
825 radiative forcing estimates in the thermal infrared. For instance, in terms of radiative
826 effect, the changes in k_{ext} may determine up to $\sim 10 \text{ W m}^{-2} \tau^{-1}$ variability in the dust
827 infrared forcing efficiency. These results point out the importance of better characterizing
828 the infrared optical properties of dust in order to more correctly evaluate their impact on
829 the climate system.

830 Spectral complex refractive index data obtained in this study are made available as
831 supplementary material to this paper for use in remote sensing and radiative transfer
832 calculations. Due to the scarcity of information on the infrared refractive index of desert dust,
833 this new dataset constitutes an important contribution for mineral dust studies on the regional
834 and global scale.

835

836 **Appendix A. Selection of dust events and identification of their source region**

837 The five dust cases analysed in this study were selected based on their different origin and
838 associated mineralogical composition. Three of them were collected at the Sahelian site of
839 Banizoumbou and the other two at the Saharan site of Tamanrasset.

840 Samples were taken during different periods corresponding to the different phases of the
841 West Africa Monsoon (WAM) annual cycle and associated AMMA Special Observing
842 Periods (SOPs). For Banizoumbou, one of the dust samples was taken during winter in
843 correspondence of the dry season (January - February 2006, AMMA SOP0; sample ID:
844 SOP0-47), and the other two during the pre-Monsoon season (June 2006, AMMA SOP1;
845 samples ID: SOP1-8 and SOP1-17). Emission of dust from the Sahel seldom occurs during
846 the dry season and aerosols collected at Banizoumbou in that period correspond to transport
847 from Saharan areas (Rajot et al., 2008). The SOP0-47 case sampled during the dry season

848 occurred on the 9th of February 2006. This case was associated to a medium-range transport
849 event originated from the Central-Western part of Niger, between the Algeria-Niger and the
850 Mali-Niger frontier regions (Klaver, 2012). In contrast with the dry season, the pre-Monsoon
851 phase is characterized by a maximum in Sahelian dust emissions (Marticorena et al. 2010).
852 Identification of erosion conditions leading to aeolian emission have been performed by
853 combining surface wind field and aerosol mass/concentration measurements, with the data on
854 sand grain horizontal flow obtained by means of a saltiphone installed in proximity of the
855 sampling site station (Klaver, 2012). Two different local erosion episodes are considered
856 from the pre-monsoon season at Banizoumbou: SOP1-8, which occurred on the 4th of June
857 2006, and SOP1-17, between the 8th and the 9th of June 2006. The SOP1-8 event was
858 identified as the strongest erosion episode of the entire SOP1 period at Banizoumbou, based
859 on the measured surface wind speed ($>10 \text{ m s}^{-1}$ during the whole event, consistently above
860 the 6 m s^{-1} threshold for local emission estimated by Rajot et al. (2008)) and horizontal dust
861 grain flux (peak at $\sim 700 \text{ counts s}^{-1}$). SOP1-17 was instead a post-erosion event characterized
862 by the advection of dust which was locally emitted at Banizoumbou ~ 3 hours before the
863 sampling started.

864 Tamanrasset data considered here have been acquired in the second part of 2006, during the
865 Monsoon season (July - August 2006, AMMA SOP2; sample ID: N32), and the end of the
866 Monsoon, during the Inter Tropical Convergence Zone (ITCZ) retreat (October – November
867 2006; sample ID: N93). As discussed by Cuesta et al. (2008), local dust production at
868 Tamanrasset (over the Hoggar massif) is very low, and most aeolian dust over this area is
869 transported from a variety of different source regions as a result of different dust lifting
870 mechanisms (e.g., low-level jets, cold pools, or topographic flows). The event considered
871 here in correspondence of the Monsoon season over the Sahel occurred between the 21st and
872 the 27th of July 2006. The dust event originated at the Algeria-Niger frontier and was caused
873 by the succession of three cold pools outflows generated by Mesoscale Convective Systems
874 (MCS). The ITD (Inter-Tropical Discontinuity) organized the three cold pools in a dust front,
875 which propagated northwards to Tamanrasset (Cuesta et al., 2009a). The N32 sample was
876 taken only in the first part of the episode, between the 23rd and the 24th of July. The origin of
877 the N93 post-Monsoon dust event over Tamanrasset, instead, was associated to an intrusion
878 of the Sub Tropical Westerly Jet (STWJ) into Morocco and North-Western Algeria, which
879 led to the formation of downslope winds along the Saharan side of Atlas Mountains. These
880 winds induced the formation of a dust front which moved southward reaching Tamanrasset

881 between the 5th and the 7th of October 2006 (N93 sample taken throughout the whole event,
882 between the 5th and the 7th of October) (see Cuesta et al., 2008 and suppl. material). For both
883 events (during and after the Monsoon season over the Sahel), the transport time from the
884 source regions to the sampling site of Tamanrasset was estimated to be about 1 day.

885

886 **Appendix B. Estimation of dust mineralogical composition.**

887 Starting from the measurements described in Section 2.2 (WD-XRF, XRD, CBD, XANES,
888 and EXAFS), the mineralogical composition of the different dust samples has been estimated
889 through the following procedure.

890 At first, the Total Dust Mass (TDM) collected on the filters has been determined. For samples
891 SOP0-47, SOP1-8, and SOP1-17, the TDM has been obtained directly from an on-line
892 Tapering Element Oscillating Microbalance (TEOM, model 1400a, Rupprecht and
893 Patashnick Albany, USA; 5% uncertainty) available at Banizoumbou (Rajot et al., 2008).
894 These measurements were not available at Tamanrasset. Another possible approach to
895 estimate the TDM consists in calculating it based on the XRF measured elemental
896 composition. XRF analysis was not possible on N32 and N93 samples due to the high amount
897 of dust particles deposited on the filters. We therefore considered four filters sampled
898 immediately before and after the N32 and N93 events. For these filters, for which elemental
899 composition was available from XRF analysis, the TDM was estimated as described in
900 Formenti et al. (2014). Co-located Level 2.0 AERONET measurements at 0.50 μm obtained
901 at Tamanrasset (Cuesta et al., 2008) allowed the estimation of an average aerosol optical
902 depth ($\bar{\tau}$) for these cases. A linear relationship ($y=bx$) between TDM and $\bar{\tau}$ can be
903 established for these filters ($R^2=0.87$) with $b = (3122 \pm 367) \mu\text{g}$. The obtained b has been then
904 used, together with the measured $\bar{\tau}$ (see Table 1), to extrapolate the TDM for the N32 and
905 N93 events. The uncertainty on the obtained TDM is $\sim 12\%$. This procedure for the estimation
906 of the TDM assumes the existence of a proportionality relation between the dust mass
907 (sampled at the ground) and the aerosol optical depth (measured over the whole atmospheric
908 column). This hypothesis can be considered valid at Tamanrasset where the distribution of
909 dust particles has been observed to be generally uniform within the so called Saharan
910 Atmospheric Boundary Layer, SABL (from a maximum altitude of ~ 6 km down to the
911 ground) (Cuesta et al., 2008 and 2009b). CALIPSO lidar transects (<http://www->

912 calipso.larc.nasa.gov/products/lidar) passing very close to Tamanrasset in correspondence
913 with the two considered dust events also confirms this assumption.

914 As a second step, the apportionment of the TDM between the different minerals has been
915 evaluated in the following way:

916 1) the mass of quartz (with an uncertainty of $\pm 3\%$), Ca-rich species (calcite, $\pm 3\%$, dolomite,
917 $\pm 10\%$, gypsum, $\pm 5\%$), and feldspars (orthose, $\pm 7\%$, albite, $\pm 2\%$) have been estimated,
918 both for the Banizoumbou and the Tamanrasset samples, from XRD analysis by applying
919 the calibration coefficients reported in Klaver et al. (2011) and Formenti et al. (2014);
920 2) the mass of iron oxides has been obtained from CBD ($\pm 10\%$) for the SOP0-47, SOP1-8,
921 and SOP1-17. For the N32 and N93 cases, instead, the iron oxide content has been
922 estimated from the elemental Fe assuming the ratio between the iron in the form of oxide
923 and the total elemental Fe to be 0.59 (Formenti et al., 2008). The Fe content of the N32
924 and N93 events has been calculated with a procedure similar to that used for the TDM, i.e.
925 by performing a linear fit ($y=dx$) of the measured Fe and $\bar{\tau}$ for the four dust samples
926 obtained before and after the two considered events. The result in this case is $d = (142 \pm$
927 $18) \mu\text{g}$, with a correlation $R^2 = 0.87$. The uncertainty on the iron oxide content estimated
928 through this procedure is $\sim 12\%$. For SOP1-17 sample only, the speciation between
929 hematite and goethite has been also determined through XANES and EXAFS analyses;
930 3) the mass of clays (kaolinite, illite, smectite, chlorite), which cannot be directly determined
931 from XRD data due to the absence of appropriated calibration standards for these
932 components, has been estimated as the difference between TDM and the total mass of
933 quartz, Ca-rich species, feldspars, and iron oxides. The mass apportionment between the
934 different clays species can be performed when only kaolinite (K) and illite (I) are present.
935 In this case the mass of the two clays can be separated by the knowledge of their ratio I/K,
936 as estimated by Caquineau et al. (2002). For SOP0-47, SOP1-8, and SOP1-17, the I/K
937 ratio was set at 0.1. For the N32 and N93 samples, instead, also smectite was detected in
938 XRD spectra and the mass apportionment between the different clay species cannot be
939 done. The uncertainty on the estimated total clay mass, calculated with the error
940 propagation formula considering the uncertainties on TDM and the other identified
941 mineral species, varies between 8 and 20%.

942

943

944

945 **Acknowledgements**

946 This work was supported by the Centre National des Etudes Spatiales (CNES). Based on a
947 French initiative, AMMA was built by an international scientific group and is currently
948 funded by a large number of agencies, especially from France, the United Kingdom, the
949 United States, and Africa. It has been the beneficiary of a major financial contribution from
950 the European Community's Sixth Framework Research Programme. Detailed information on
951 scientific coordination and funding is available on the AMMA International Web site at
952 www.amma-international.org. The Tamanrasset AMMA supersite deployment and operation
953 were supported by the Office National de la Météorologie (ONM) in Algeria, the Laboratoire
954 de Météorologie Dynamique (LMD), and the Laboratoire Atmosphères, Milieux,
955 Observations Spatiales (LATMOS). Thanks are also due to the LISA personnel who
956 participated in field campaigns and helped with sample collection and analyses. Helpful
957 comments and suggestions by two anonymous reviewers are also acknowledged.

958

959

960

961

962

963

964

965

966

967

968

969

970

971

972

973

974

975

976

977 **References**

978 Ackerman, S. A., and Chung, H.: Radiative effects of airborne dust on regional energy budgets at the
979 top of the atmosphere, *J. Appl. Meteorol.*, 31, 223–233, 1992.

980 Ackerman, S. A.: Remote sensing aerosols using satellite infrared observations, *J. Geophys. Res.*,
981 102, 17,069– 17,080, 1997.

982 Balkanski, Y., Schulz, M., Clauquin, T., and Guibert, S.: Reevaluation of Mineral aerosol radiative
983 forcings suggests a better agreement with satellite and AERONET data, *Atmos. Chem. Phys.*, 7,
984 81–95, doi:10.5194/acp-7-81-2007, 2007.

985 Banks, J. R., and Brindley, H. E.: Evaluation of MSG-SEVIRI mineral dust retrieval products over
986 North Africa and the Middle East, *Rem. Sens. Environ.*, 128, 58-73, 2013.

987 Ben-Ami, Y., Koren, I., and Altaratz, O.: Patterns of North African dust transport over the Atlantic:
988 winter vs. summer, based on CALIPSO first year data, *Atmos. Chem. Phys.*, 9, 7867-7875,
989 10.5194/acp-9-7867-2009, 2009.

990 Ben-Ami, Y., Koren, I., Rudich, Y., Artaxo, P., Martin, S. T., and Andreae, M. O.: Transport of North
991 African dust from the Bodele depression to the Amazon Basin: a case study, *Atmos. Chem. Phys.*,
992 10, 7533–7544, 2010.

993 Bierwirth, E., Wendisch, M., Ehlich, A., Heese, B., Tesche, M., Althausen, D., Schladitz, A., Müller,
994 D., Otto, S., Trautmann, T., Dinter, T., Von Hoyningen-Huene, W., and Kahn, R.: Spectral
995 surface albedo over Morocco and its impact on radiative forcing of Saharan dust, *TellusB*, 61,
996 252–269, 2009.

997 Bohren, C. E., and Huffman, D. R.: *Absorption and Scattering of Light by Small Particles*. Wiley,
998 New York, 1983.

999 Brindley, H. E., and Russell, J. E.: An assessment of Saharan dust loading and the corresponding
1000 cloud-free longwave direct radiative effect from geostationary satellite observations, *J. Geophys.*
1001 *Res.*, 114, D23201, doi:10.1029/2008JD011635, 2009.

1002 Capelle, V., Chédin, A., Siméon, M., Tsamalis, C., Pierangelo, C., Pondrom, M., Armante, R.,
1003 Crevoisier, C., Crepeau, L., and Scott, N. A.: Evaluation of IASI derived dust aerosols
1004 characteristics over the tropical belt, *Atmos. Chem. Phys. Discuss.*, 13, 30143-30186,
1005 doi:10.5194/acpd-13-30143-2013, 2013.

1006 Caquineau, S., Magonthier, M. C., Gaudichet, A., and Gomes, L.: An improved procedure for the X-
1007 ray diffraction analysis of low-mass atmospheric dust samples, *Eur. J. Mineral.*, 9, 157–166:
1008 1997.

1009 Caquineau, S., Gaudichet, A., Gomes, L., and Legrand, M.: Mineralogy of Saharan dust transported
1010 over northwestern tropical Atlantic Ocean in relation to source regions, *J. Geophys. Res.*,
1011 107(D15), 4251, doi:10.1029/2000JD000247. 2002.

1012 Carlson, T. N., and Benjamin, ST. G.: Radiative heating rates for Saharan dust, *J. Atmos. Sc.*, 193-
1013 213, 1980.

1014 Carslaw, K. S., Boucher, O., Spracklen, D. V., Mann, G. W., Rae, J. G. L., Woodward, S., and
1015 Kulmala, M.: A review of natural aerosol interactions and feedbacks within the Earth system,
1016 *Atmos. Chem. Phys.*, 10, 1701-1737, doi:10.5194/acp-10-1701-2010, 2010.

1017 Casasanta, G., di Sarra, A. G., Meloni, D., Monteleone, F., Pace, G., Piacentino, S, and Sferlazzo, D:
1018 Large aerosol effects on ozone photolysis in the Mediterranean, *Atmos. Env.*, 45, 3937-3943,
1019 2011.

1020 Chan, P. K., and Gao, B. J.: A comparison of MODIS, NCEP, and TMI sea surface temperature
1021 datasets, *IEEE Geosci. Remote Sens. Lett.*, 2(3), 270-274,doi: 10.1109/LGRS.2005.846838,
1022 2005.

1023 Clauquin, T., Schulz, M., Balkanski, Y. J., and Boucher, O.: Uncertainties in assessing radiative
1024 forcing by mineral dust, *TellusB*, 50, 491–505, 1998.

1025 Clauquin, T., Schulz, M., and Balkanski, Y. J.: Modeling the mineralogy of atmospheric dust sources.,
1026 *J. Geophys. Res.*, 104, 22243-22256, 1999.

1027 Cuesta, J., Edouart, D., Mimouni, M., Flamant, P. H., Loth, C., Gibert, F., Marnas, F., Bouklila, A.,
1028 Kharef, M., Ouchène, B., Kadi, M., and Flamant, C.: Multiplatform observations of the seasonal
1029 evolution of the Saharan atmospheric boundary layer in Tamanrasset, Algeria, in the framework

1030 of the African Monsoon Multidisciplinary Analysis field campaign conducted in 2006, *J.
1031 Geophys. Res.*, 113, D00C07, doi:10.1029/2007JD009417, 2008.

1032 Cuesta, J. Lavaysse, C., Flamant, C., Mimouni, M., and Knippertz, P.: Northward bursts of the West
1033 African monsoon leading to rainfall over the Hoggar Massif, Algeria, *Q. J. R. Meteorol. Soc.*,
1034 doi: 10.1002/qj.439, 2009a.

1035 Cuesta, J., Marsham, J. H., Parker, D. J., and Flamant, C.: Dynamical mechanisms controlling the
1036 vertical redistribution of dust and the thermodynamic structure of the West Saharan atmospheric
1037 boundary layer during summer, *Atmos. Sci. Lett.*, 10: 34–42, 2009b.

1038 D'Almeida, G. A., Koepke, P., and Shettle, E. P.: *Atmospheric Aerosols: Global Climatology and
1039 Radiative Characteristics*, A. Deepak Publishing, 561 pp., 1991.

1040 DeSouza-Machado, S. G., Strow, L. L., Hannon, S. E., and Motteler, H. E.: Infrared dust spectral
1041 signatures from AIRS, *Geophys. Res. Lett.*, 33(L03801), 1-5, 2006.

1042 Di Biagio, C., di Sarra, A., and Meloni, D.: Large atmospheric shortwave radiative forcing by
1043 Mediterranean aerosol derived from simultaneous ground-based and spaceborne observations,
1044 and dependence on the aerosol type and single scattering albedo, *J. Geophys. Res.*, 115, D10209,
1045 doi:10.1029/2009JD012697, 2010.

1046 di Sarra, A., Di Biagio, C., Meloni, D., Monteleone, F., Pace, G., Pugnaghi, S., and Sferlazzo, D.:
1047 Shortwave and longwave radiative effects of the intense Saharan dust event of March 25-26,
1048 2010, at Lampedusa (Mediterranean sea), *J. Geophys. Res.*, 116, D23209,
1049 doi:10.1029/2011JD016238, 2011.

1050 Dufresne, J.-L., Gautier, C., Ricchiazzi, P., and Fouquart, Y.: Longwave scattering effects of mineral
1051 aerosols, *J. Atmos. Sci.*, 59, 1959–1966, 2002.

1052 Fisher, K.: The optical constants of atmospheric aerosol particles in the 7.5 - 12 μm spectral region,
1053 *Tellus*, XXVIII, 266- 274, 1976.

1054 Formenti, P., Rajot, J. L., Desboeufs, K., Caquineau, S., Chevaillier, S., Nava, S., Gaudichet, A.,
1055 Journet, E., Triquet, S., Alfaro, S., Chiari, M., Haywood, J., Coe, H., and Highwood, E.:
1056 Regional variability of the composition of mineral dust from western Africa: Results from the
1057 AMMA SOP0/DABEX and DODO field campaigns, *J. Geophys. Res.*, 113, D00C13,
1058 10.1029/2008jd009903, 2008.

1059 Formenti, P., Schütz, L., Balkanski, Y., Desboeufs, K., Ebert, M., Kandler, K., Petzold, A.,
1060 Scheuvens, D., Weinbruch, S., and Zhang, D.: Recent progress in understanding physical and
1061 chemical properties of African and Asian mineral dust, *Atmos. Chem. Phys.*, 11, 8231-8256,
1062 10.5194/acp-11-8231-2011, 2011a.

1063 Formenti, P., Caquineau, S., Desboeufs, K., Klaver, A., Chevaillier, S., Journet, E., and Rajot, J.L.:
1064 Mapping the physico-chemical properties of mineral dust in Western Africa: Mineralogical
1065 composition, submitted to *Atmos. Chem. Phys. Discuss.*, 2014.

1066 Fouquart, Y., Bonnel, B., Brogniez, G., Buriez, J. C., Smith, L., Morcrette, J. J.: Observations of
1067 Sahara aerosols: Results of ECLATS field experiment. Part II: Broadband radiative
1068 characteristics of the aerosols and vertical radiative flux divergence, *J. Climate Appl. Meteor.* 26,
1069 38-52, 1987.

1070 Fratini, G., Ciccioli, P., Febo, A., Forgione, A. and Valentini, R.: Size-segregated fluxes of mineral
1071 dust from a desert area of northern China by eddy covariance, *Atmos. Chem. Phys.* 7, 2839–
1072 2854, 2007.

1073 Ginoux, P., Prospero, J. M., Gill, T. E., Hsu, N. C., and Zhao, M.: Global-scale attribution of
1074 anthropogenic and natural dust sources and their emission rates based on MODIS Deep Blue
1075 aerosol products, *Rev. Geophys.*, 50, RG3005, doi:10.1029/2012RG000388, 2012.

1076 Glotch, T. D., Rossman, G.R., and Aharonson, O.: Mid-infrared (5–100 μm) reflectance spectra and
1077 optical constants of ten phyllosilicate minerals, *Icarus*. 192 : 604–622, 2007.

1078 Glotch T. D., and Rossman, G. R.: Mid-infrared reflectance spectra and optical constants of six iron
1079 oxide/oxyhydroxide phases, *Icarus* 204 : 663–671, 2009.

1080 Gomes, L., and Gillette, D. A.: A comparison of characteristics of aerosol from dust storms in central
1081 Asia with soil-derived dust from other regions, *Atmos. Environ.*, 27A, 2539-2544.1993.

1082 Hansell, Jr., R. A., Reid, J. S., Tsay, S. C., Roush, T. L., and Kalashnikova, O. V.: A sensitivity study
1083 on the effects of particle chemistry, asphericity and size on the mass extinction efficiency of

1084 mineral dust in the earth's atmosphere: from the near to thermal IR, *Atmos. Chem. Phys.*, 11,
1085 1527-1547, doi:10.5194/acp-11-1527-2011, 2011.

1086 Haywood, J., Francis, P., Osborne, S., Glew, M., Loeb, N., Highwood, E., Tanré, D., Myhre, G.,
1087 Formenti, P., and Hirst, E.: Radiative properties and direct radiative effect of Saharan dust
1088 measured by the C-130 aircraft during SHADE: 1. Solar spectrum, *J. Geophys. Res.*, 108(D18),
1089 8577, doi:10.1029/2002JD002687, 2003.

1090 Haywood, J. M., Allan, R. P., Slingo, T., Milton, S., Edwards, J., and Clerbaux, N.: Can desert dust
1091 explain the outgoing longwave radiation anomaly over the Sahara during July 2003?, *J. Geophys.*
1092 *Res.*, 110, D05105, doi:10.1029/2004JD005232, 2005.

1093 Heim, M., Mullins, B. J., Umhauer, H., Kasper, G.: Performance evaluation of three optical particle
1094 counters with an efficient “multimodal” calibration method, *J. Aer. Sci.*, 39, 1019-1031, 2008.

1095 Heinold, B., Tegen, I., Schepanski, K., and Hellmuth, O.: Dust radiative feedback on Saharan
1096 boundary layer dynamics and dust mobilization, *Geophys. Res. Lett.*, 35, L20817,
1097 doi:10.1029/2008GL035319, 2008.

1098 Hess, M., Koepke, P., and Schult, I.: Optical properties of aerosols and clouds: The software package
1099 OPAC, *Bull. Am. Meteorol. Soc.*, 79, 831–844, 1998.

1100 Highwood, E. J., Haywood, J. M., Silverstone, M. D., Newman, S. M., and Taylor, J. P.: Radiative
1101 properties and direct effect of Saharan dust measured by the C-130 aircraft during Saharan Dust
1102 Experiment (SHADE): 2. Terrestrial spectrum, *J. Geophys. Res.*, 108(D18), 8578,
1103 doi:10.1029/2002JD002552, 2003.

1104 Hsu, N. C., Herman, J. R., and Weaver, C. J.: Determination of radiative forcing of Saharan dust
1105 using combined TOMS and ERBE data, *J. Geophys. Res.*, 105(D16), 20,649–20,661,
1106 doi:10.1029/2000JD900150, 2000.

1107 Hudson, P. K., Gibson, E. R., Young, M. A., Kleiber, P. D., and Grassian V. H.: Coupled infrared
1108 extinction and size distribution measurements for several clay components of mineral dust
1109 aerosol, *J. Geophys. Res.*, 113, D01201, doi:10.1029/2007JD008791, 2008a.

1110 Hudson, P. K., Young, M. A., Kleiber, P. D., and Grassian, V. H.: Coupled infrared extinction spectra
1111 and size distribution measurements for several non-clay components of mineral dust aerosol
1112 (quartz, calcite, and dolomite), *Atmos. Environ.*, 42(24), 5991–5999,
1113 doi:10.1016/j.atmosenv.2008.03.046, 2008b.

1114 Huneeus, N., Chevallier, F. and Boucher, O.: Estimating aerosol emissions by assimilating observed
1115 aerosol optical depth in a global aerosol model, *Atmos. Chem. Phys.*, 12, 4585–4606, 2012.

1116 Israelevich, P. L., Levin, Z., Joseph, J. H., and Ganor, E.: Desert aerosol transport in the
1117 Mediterranean region as inferred from the TOMS aerosol index, *J. Geophys. Res.*, 107, 4572,
1118 doi:10.1029/2001jd002011, 2002.

1119 Iwasaka, Y., Shi, G.-Y. Shen, Z., Kim, S., Trochkin, D., et al.: Nature of atmospheric aerosols over
1120 the desert area in the Asian continent: chemical state and number concentration of particles
1121 measured at Dunhuang, China, *Water, Air Soil Pollut.: Focus* 3, 129–145, 2003.

1122 Kalashnikova, O. V., and Sokolik, I. N.: Importance of shapes and compositions of wind-blown dust
1123 particles for remote sensing at solar wavelengths, *Geophys. Res. Lett.*, 29, 10, 2002.

1124 Kandler, K., Schütz, L., Deutscher, C., Ebert, M., Hofmann, H., Jäckel, S., Jaenicke, R., Knippertz, P.,
1125 Lieke, K., Massling, A., Petzold, A., Schladitz, A., Weinzierl, B., Wiedensohler, A., Zorn, S., and
1126 Weinbruch, S.: Size distribution, mass concentration, chemical and mineralogical composition
1127 and derived optical parameters of the boundary layer aerosol at Tinfou, Morocco, during
1128 SAMUM 2006, *Tellus B*, 61, 32–50, doi:10.1111/j.1600-0889.2008.00385.x, 2009.

1129 Kishcha, P., Alpert, P., Barkan, J., Kirchner, I., and Machenhauer, B.: Atmospheric response to
1130 Saharan dust deduced from ECMWF reanalysis (ERA) temperature increments, *TellusB*, 55,
1131 901–913, 2003.

1132 Klaver, A., Formenti, P., Caquineau, S., Chevaillier, S., Ausset, P., Calzolai, G., Osborne, S.,
1133 Johnson, B., Harrison, M., and Dubovik, O.: Physico-chemical and optical properties of Sahelian
1134 and Saharan mineral dust: in situ measurements during the GERBILS campaign, *Q. J. R.*
1135 *Meteorol. Soc.*, 137, 1193-1210, 10.1002/qj.889, 2011.

1136 Klaver, A.: Estimation des propriétés optiques des poussières désertiques d'origines saharienne et
1137 sahélienne, à proximité de leurs zones sources d'émission, à partir de leurs propriétés physico-
1138 chimiques, PhD thesis, Université Paris VII, 2012.

1139 Klüser, L., and Holzer-Popp, T.: Relationships between mineral dust and cloud properties in the West
1140 African Sahel, *Atmos. Chem. Phys.*, 10, 6901–6915, doi:10.5194/acp-10-6901-2010, 2010.

1141 Klüser, L., Martynenko, D., and Holzer-Popp, T.: Thermal infrared remote sensing of mineral dust
1142 over land and ocean: a spectral SVD based retrieval approach for IASI, *Atmos. Meas. Tech.*, 4,
1143 757–773, 2011.

1144 Klüser, L., Kleiber, P., Holzer-Popp, T., and Grassian, V. H.: Desert Dust Observation From Space –
1145 Application of Measured Mineral Component Infrared Extinction Spectra, *Atmos. Environ.*, 54,
1146 419–427, 2012.

1147 Koepke, P., Hess, M., Schult, I., and Shettle, E. P.: Global aerosol dataset, Report N 243, Max-Plank-
1148 Institut für Meteorologie, Hamburg, 44 pp., 1997.

1149 Lafon S., Rajot, J. L., Alfaro, S. C., and Gaudichet, A.: Quantification of iron oxides in desert aerosol,
1150 *Atmos. Environ.*, 38, 1211–1218, 2004.

1151 Laskina, O., Young, M. A., Kleiber, P. D., and Grassian, V. H.: Infrared extinction spectra of mineral
1152 dust aerosol: Single components and complex mixtures, *J. Geophys. Res.*, 117, D18210,
1153 doi:10.1029/2012JD017756, 2012.

1154 Laurent, B., Marticorena, B., Bergametti, G., Léon, J. F., and Mahowald, N. M.: Modeling mineral
1155 dust emissions from the Sahara desert using new surface properties and soil database, *J. Geophys. Res.*, 113, D14218,
1156 10.1029/2007jd009484, 2008.

1157 Legrand M., Plana-Fatto, A., and N'Doumé, C.: Satellite detection of dust using the IR imagery of
1158 Meteosat1. Infrared difference dust index, *J. Geophys. Res.*, 106 : 18251–18274, 2001.

1159 Levin, Z., and Lindberg, J.D.: Size distribution, chemical composition and optical properties of urban
1160 and desert aerosols in Israel, *J. Geophys. Res.*, 84, 6941–6950, 1979.

1161 Liu, Y. and Daum, P.: The effect of refractive index on size distributions and light scattering
1162 coefficients derived from optical particle counters, *J. Aerosol Sci.*, 31, 945–957, 2000.

1163 Long L. L., Querry, M. R., Bell, R. J., and Alexander, R. W.: Optical properties of calcite and gypsum
1164 in crystalline and powdered form in the infrared and far-infrared, *Infrared Physics*, 34, 191–201,
1165 1993.

1166 Longtin, D. R., Shettle, E. P., Hummel, J. R. and Pryce, J. D.: A Wind Dependent Desert Aerosol
1167 Model: Radiative Properties, AFGL-TR-88-0112, Air Force Geophysics Laboratory, Hanscom
1168 AFB, MA, 1988.

1169 Maring, H., Savoie, D. L., Izaguirre, M. A., McCormick, C., Arimoto, R., Prospero, J. M., and Pilinis,
1170 C.: Aerosol physical and optical properties and their relationship to aerosol composition in the
1171 free troposphere at izana, tenerife, canary islands, during July 1995, *J. Geophys. Res.-Atmos.*,
1172 105, 14677–14700, 2000.

1173 Maring, H., Savoie, D. L., Izaguirre, M. A., Custals, L., and Reid, J. S.: Mineral dust aerosol size
1174 distribution change during atmospheric transport, *J. Geophys. Res.*, 108, 8592,
1175 doi:10.1029/2002jd002536, 2003.

1176 Marra, A. C., Blanco, A., Fonti, S., Jurewicz, A., and Orofino, V.: Fine hematite particles of Martian
1177 interest: absorption spectra and optical constants, *Journal of Physics: Conference Series*, 6, 132–
1178 138, 2005.

1179 Marticorena, B., and Bergametti, G.: Modeling the atmospheric dust cycle: 1. Design of a soil-derived
1180 dust emission scheme, *J. Geophys. Res.*, 100, 16415–16430, 10.1029/95jd00690, 1995.

1181 Marticorena, B., Chatenet, B., Rajot, J. L., Traoré, S., Coulibaly, M., Diallo, A., Koné, I., Maman, A.,
1182 Ndiaye, T., and Zakou, A.: Temporal variability of mineral dust concentrations over West Africa:
1183 analyses of a pluriannual monitoring from the AMMA Sahelian Dust Transect, *Atmos. Chem. Phys.*, 10, 8899–8915,
1184 10.5194/acp-10-8899-2010, 2010.

1185 Marzo, G. A., Blanco, A., De Carlo, F., D'Elia, M., Fonti, S., Marra, A. C., Orofino, V., and Politi,
1186 R.: The Optical constants of gypsum particles as analog of Martian sulfates, *Adv. Sp. Res.*, 33,
1187 2246–2251, 2004.

1188 May, D. A., Stowe, L. L., Hawkins, J. D., and McClain, E. P.: A correction for Saharan dust effects
1189 on satellite sea surface temperature measurements, *J. Geophys. Res.*, 97(C3), 3611–3619,
1190 doi:10.1029/91JC02987, 1992.

1191 McConnell, C. L., Formenti, P. Highwood, E. J., and Harrison, M. A.: Using aircraft measurements to
1192 determine the refractive index of Saharan dust during the DODO Experiments, *Atmos. Chem. Phys.*, 10, 3081–3098,
1193 doi:10.5194/acp-10-3081-2010, 2010.

1194 Merchant, C. J., Embury, O., Le Borgne, P., and Bellec, B.: Saharan dust in nighttime thermal
1195 imagery: Detection and reduction of related biases in retrieved sea surface temperature, *Rem.*
1196 *Sens. Environ.*, 104 (1), 15-30, doi: 10.1016/j.rse.2006.03.007, 2006.

1197 Mishchenko, M. I., Liu, L., Travis, L. D., and Lacis, A. A.: Scattering and radiative properties of
1198 semi-external versus external mixtures of different aerosol types, *J. Quant. Spectrosc. Ra.*, 88,
1199 139–147, 2004.

1200 Mooney, T., and Knacke, R.F.: Optical constants of chlorite and serpentine between 2.5 and 50 μm ,
1201 *Icarus*, 64, 493-502, 1985.

1202 Nousiainen, T.: Optical modeling of mineral dust particles: A review, *J. Quant. Spectrosc. Ra.*, 110,
1203 1261–1279, 2009.

1204 Orofino, V., Blanco, A., Fonti, S., Proce, R., and Rotundi, A.: The infrared optical constants of
1205 limestone particles and implications for the search of carbonates on Mars. *Planet. Space Sci.* 46,
1206 1659–1669, 1998.

1207 Osborne, S. R., Johnson, B. T., Haywood, J. M., Baran, A. J., Harrison, M. A. J., and McConnell, C.
1208 L.: Physical and optical properties of mineral dust aerosol during the Dust and Biomass-burning
1209 Experiment, *J. Geophys. Res.*, 113, D00C03, doi:10.1029/2007jd009551, 2008.

1210 Otto, S., de Reus, M., Trautmann, T., Thomas, A., Wendisch, M., and Borrman, S.: Atmospheric
1211 radiative effects of an in situ measured Saharan dust plume and the role of large particles, *Atmos.*
1212 *Chem. Phys.*, 7, 4887–4903, 2007.

1213 Patterson, E. M., Optical Properties of the Crustal Aerosol Relation to Chemical and Physical
1214 Characteristics, *J. Geophys. Res.*, 86, 3236-3246, 1981.

1215 Peterson, J. T., and Weinman, J. A.: Optical properties of quartz dust particles at infrared
1216 wavelengths, *Geophys. Res. Lett.*, 74, 6947-6952, 1969.

1217 Petzold, A., Rasp, K., Weinzierl, B., Esselborn, M., Hamburger, T., Dörnbrack, A., Kandler, K.,
1218 Schötz, L., Knippertz, P., Fiebig, M., and Virkkula, A.: Saharan dust absorption and refractive
1219 index from aircraft-based observations during SAMUM 2006, *Tellus B*, 61, 118–130,
1220 doi:10.1111/j.1600-0889.2008.00383.x, 2009.

1221 Pierangelo, C., Chédin, A., Heilliette, S., Jacquinot-Husson, N., and Armante, R.: Dust altitude and
1222 infrared optical depth from AIRS, *Atmos. Chem. Phys.*, 4, 1813–1822, 2004.

1223 Prospero, J. M., Ginoux, P., Torres, O., Nicholson, S. E., and Gill, T. E.: Environmental
1224 characterization of global sources of atmospheric soil dust identified with the Nimbus 7 Total
1225 Ozone Mapping Spectrometer (TOMS) absorbing aerosol product, *Rev. Geophys.*, 40, 2-1–2-31,
1226 2002.

1227 Pujol, J.: The solution of nonlinear inverse problems and the Levenberg-Marquardt method,
1228 *Geophysics* (SEG) 72 (4): W1–W16. doi:10.1190/1.2732552, 2007.

1229 Pye, K.: Aeolian Dust and Dust Deposits, Academic Press, London, 334 pp., 1987.

1230 Querry, M. R., Osborne, G., Lies, K., Jordon, R., Coveney, R. M.: Complex refractive index of
1231 limestone, *Appl. Opt.*, 17, 353–356, 1978, 1978.

1232 Querry, M.: Optical Constants of Minerals and Other Materials from the Millimeter to the Ultraviolet,
1233 Report CRDEC-CR-88009, US Army, Aberdeen, 1987.

1234 Rajot, J. L., Formenti, P., Alfaro, S., Desboeufs, K., Chevaillier, S., Chatenet, B., Gaudichet, A.,
1235 Journet, E., Marticorena, B., Triquet, S., Maman, A., Mouget, N., and Zakou, A.: AMMA dust
1236 experiment: An overview of measurements performed during the dry season special observation
1237 period (SOP0) at the Banizoumbou (Niger) supersite, *J. Geophys. Res.*, 113, D00C14,
1238 doi:10.1029/2008jd009906, 2008.

1239 Redelsperger, J.-L., Thorncroft, C. D., Diedhiou, A., Lebel, T., Parker, D. J., and Polcher, J.: African
1240 Monsoon Multidisciplinary Analysis: An International Research Project and Field Campaign, *B.*
1241 *Am. Meteorol. Soc.*, 87, 1739–1746, doi:10.1175/BAMS-87-12-1739, 2006.

1242 Reid, E. A., Reid, J. S., Meier, M. M., Dunlap, M. R., Cliff, S. S., Broumas, A., Perry, K., and
1243 Maring, H.: Characterization of African dust transported to Puerto Rico by individual particle
1244 and size segregated bulk analysis, *J. Geophys. Res.*, 108, 8591, 10.1029/2002jd002935, 2003.

1245 Rosenfeld, D., Rudich, Y, and Lahav, R.: Desert dust suppressing precipitation: A possible
1246 desertification feedback loop, *Proc. Natl. Acad. Sci. U. S. A.*, 98, 5975–5980,
1247 doi:10.1073/pnas.101122798, 2001.

1248 Roush, T., Pollack, J., and Orenberg, J.: Derivation of midinfrared (5–25 μm) optical constants of
1249 some silicates and palagonite. *Icarus* 94, 191–208, 1991.

1250 Saikia, B., and Parthasarathy, G.: Fourier Transform Infrared Spectroscopic Characterization of
1251 Kaolinite from Assam and Meghalaya, Northeastern India, *J. Mod. Phys.*, 2010, 1, 206-210,
1252 2010.

1253 Schütz, L., Jaenicke, R., and Pietrek, H.: Saharan dust transport over the North Atlantic Ocean, *Spec.*
1254 *Pap. Geol. Soc. Am.*, 186, 87–100, 1981.

1255 Shettle, E. P. and Fenn, R. W.: Models of the atmospheric aerosols and their optical properties, in
1256 AGARD Conference Proceedings n. 183, Optical Propagation in the Atmosphere. Presented at
1257 the Electromagnetic Wave Propagation Panel Symposium. Lyngby, Denmark, 27-31 October
1258 1975. AGARD-CP-183, available from U.S. National Technical Information Service, AD A028-
1259 615, 1976.

1260 Shettle, E. P. and Fenn, R. W.: Models for the Aerosols of the Lower Atmosphere and the Effects of
1261 Humidity Variations on Their Optical Properties, AFGL-TR-79-0214, ADA085951, 1979.

1262 Slingo, A., Ackerman, T. P., Allan, R. P., Kassianov, E. I., McFarlane, S. A., Robinson, G. J.,
1263 Barnard, J. C., Miller, M. A., Harries, J. E., Russell, J. E., and Dewitte, S.: Observations of the
1264 impact of a major Saharan dust storm on the atmospheric radiation balance, *Geophys. Res. Lett.*,
1265 33, L24817, doi:10.1029/2006GL027869, 2006.

1266 Sokolik, I. N., Andronova, A., and Johnson, T. C.: Complex refractive index of atmospheric dust
1267 aerosols, *Atmos. Env.*, 27A, 2495-2502, 1993.

1268 Sokolik, I. N., and Toon, O. B.: Direct radiative forcing by anthropogenic airborne mineral aerosols,
1269 *Nature*, 381, 681-683, doi: 10.1038/381681a0, 1996.

1270 Sokolik, I. N., Toon, O. B., Bergstrom, R. W.: Modeling the radiative characteristics of airborne
1271 mineral aerosols at infrared wavelengths. *Journal of Geophysical Research Letters*. 103 : 8813-
1272 8826, 1998.

1273 Sokolik, I., and Toon, O.: Incorporation of mineralogical composition into models of the radiative
1274 properties of mineral aerosol from UV to IR wavelengths, *J. Geophys. Res.*, 104, 9423-9444,
1275 1999.

1276 Sokolik, I. N.: The spectral radiative signature of wind-blown mineral dust: Implications for remote
1277 sensing in the thermal IR region, *Geophys. Res. Lett.*, 29(24), 2154,
1278 doi:10.1029/2002GL015910, 2002.

1279 Spitzer, W.G., and Kleinman, D.A.: Infrared lattice bands of quartz. *Phys. Rev.* 121, 1324–1335,
1280 1961.

1281 Textor, C., et al.: The effect of harmonized emissions on aerosol properties in global models: an
1282 AeroCom experiment, *Atmos. Chem. Phys.*, 7, 4489–4501, doi:10.5194/acp-7-4489-2007, 2007.

1283 Toon, O. B., and Pollack, J. B.: A global average model of atmospheric aerosols for radiative transfer
1284 calculations, *J. Appl. Meteor.*, 15: 225-246, 1976.

1285 Volz F.E.: Infrared refractive index of atmospheric aerosol substances, *Appl. Optics*, 11, 755-759,
1286 1972.

1287 Volz, F. E.: Infrared optical constants of ammonium sulfate, Sahara dust; volcanic pumice and flyash,
1288 *Appl. Optics*, 12, 564-568, 1973.

1289 Wang, H., Shi, G., Li., S., Li., W., Wang, B., and Huang, Y.: The impact of optical properties on
1290 radiative forcing due to dust aerosols, *Adv. Atm. Sci.*, 23, 431-441, 2006.

1291 World Meteorology Organization (WMO) publication. World Climate Research Program: A
1292 preliminary cloudless standard atmosphere for radiation computation, WCP-112, WMO/TD-NO.
1293 24, 1986.

1294 Winfield, K. A.: Factors controlling water retention of alluvial deposits. Western Mojave Desert,
1295 available at <http://wwwrcamnl.wr.usgs.gov/uzf/winfield.thesis.pdf>. *Tellus*, 2000.

1296

1297

1298

1299

1300

1301

1302 **Table captions**

1303

1304 **Table 1.** Main characteristics of the five dust cases selected in this study: the sample ID, the
1305 measurement site, the date and time of beginning and end of the observed dust event, the
1306 associated filter sampling time interval within the event, and the identified dust source region.
1307 The mean aerosol optical depth (τ) at 0.50 μm and the Ångstrom exponent (α , calculated
1308 between 0.44 and 0.87 μm) obtained from AERONET measurements during filter sampling
1309 for the different cases are also reported; no data are available for the SOP1-8, when the solar
1310 zenith angle at the sampling start was $>70^\circ$, and for the SOP1-17, which corresponds to
1311 nighttime data.

1312

1313 **Table 2.** Mineralogical composition (% by mass) of the five samples from the Banizoumbou
1314 and the Tamanrasset sites. The estimated uncertainties associated to the identification of the
1315 different mineral species are: clays ($\pm 8\text{--}20\%$), quartz ($\pm 3\%$), calcite ($\pm 3\%$), dolomite ($\pm 10\%$),
1316 gypsum ($\pm 5\%$), orthose ($\pm 7\%$), albite ($\pm 2\%$), iron oxides ($\pm 10\text{--}12\%$).

1317

1318 **Table 3.** Position of main detected dust infrared band peaks with associated mineral specie
1319 and transition assignment.

1320

1321 **Table 4.** Estimated dust optical depth and TOA forcing efficiency (FE, $\text{W m}^{-2} \tau^{-1}$) at 8, 10,
1322 and 12 μm for the SOP0-47, N32, and N93 cases (see text for details). The measured τ at 0.50
1323 μm from AERONET is also reported.

1324

1325 **Figure captions**

1326

1327 **Figure 1.** Particle number ($dN/d\log D$) and volume ($dV/d\log D$) size distributions (normalized
1328 with respect to the total number and total volume of particles, respectively) obtained for the
1329 five selected dust events. The dots indicate the GRIMM measured values, while the lines are
1330 the multimodal lognormal fits data. Black and grey dashed lines are the averages of the
1331 volume size distributions for the five samples obtained including (mean_A, black dashed
1332 line) and excluding (mean_B, grey dashed line) the largest mode at $\sim 25 \mu\text{m}$ for N32 and N93
1333 samples. The legend in bottom panel identifies the line styles used in the plot.

1334

1335

1336 **Figure 2.** Absorbance spectra measured in the spectral range 2.5-25 μm for the five different
1337 dust samples. The legend identifies the line styles used in the plot.

1338

1339

1340 **Figure 3.** Real (n) and imaginary (k) parts of the complex refractive index in the spectral
1341 range 2.5-25 μm for individual minerals composing dust. References for the plotted curves
1342 are: kaolinite (Glotch et al., 2007); illite (Querry, 1987); montmorillonite (a mineral of the
1343 smectite family, taken here as representative for this clay species) (Glotch et al., 2007);
1344 quartz (Peterson and Weimnman, 1969); calcite (Querry et al., 1978; Long et al., 1993);
1345 dolomite (Querry, 1987); gypsum (Long et al., 1993); hematite (Marra et al., 2005); goethite
1346 (Glotch and Rossman, 2009). No literature data are available for feldspars (orthose and
1347 albite) at infrared wavelengths. The colour code used for the different minerals is indicated in
the legend.

1348
1349
1350
1351
1352
1353

Figure 4. Comparison between the experimental $Q_{\text{abs}}(\lambda)/a$ (cm^{-1}) spectra (black curves) and the theoretical ones obtained from the nonlinear fitting procedure (yellow curves). The line styles used in the plot and the number of oscillators for each fit are also indicated in the legend.

1353

1354 **Figure 5.** Residuals ($R = \frac{(\text{exp} - \text{fit})}{\sigma_{\text{exp}}}$) of the fit normalized by the measurement errors
1355 calculated for SOP1-8 and N93. In the residual calculation, exp is the experimental $Q_{\text{abs}}(\lambda)/a$,
1356 while fit is the $Q_{\text{abs}}(\lambda)/a$ obtained from the fitting procedure. The measurement error, σ_{exp} , is
1357 6.4% for SOP1-8 and 5.9% for N93. Red lines indicate the ± 1 interval.
1358

1359 **Figure 6.** Real (n, top panel) and imaginary (k, bottom panel) part of the complex refractive
1360 index obtained in the range $2.5 - 25 \mu\text{m}$ for the five different dust samples. The legend
1361 identifies the line styles used in the plot.
1362

1363 **Figure 7.** Comparison of our results with other direct and indirect estimates of the dust
1364 refractive index as reported in the literature. The plot reports the real and the imaginary parts
1365 of the refractive index for: 1. *Volz (1972)* (indicated as VO72 in the plot): rainout dust
1366 aerosols collected in Germany and composed of a mixture of soil particles, fly ashes, and
1367 pollen (spectroscopy method; also used as the “dust-like” model in Shettle and Fenn, 1979);
1368 2. *Volz (1973)* (indicated as VO73): Saharan dust collected at Barbados, West Indies
1369 (spectroscopy method); 3. *Fouquart et al. (1987)* (indicated as FO87): Saharan sand collected
1370 at Niamey, Niger (spectroscopy method); 4. *Carlson and Benjamin, (1980), Sokolik et al.*
1371 (1993) (indicated as CA80): mineral dust model, as used in the OPAC and GADS databases
1372 (based on a synthesis of measurements on Saharan dust or generally on desert aerosols); 5.
1373 *Longtin et al. (1988)* (indicated as LO88): dust sand, i.e. modelled as an internal mixture of
1374 hematite (10% by volume) and quartz. In the internal mixing hypothesis the dust refractive
1375 index is calculated as the volume average of the refractive indices of individual minerals; 6.
1376 *OPAC desert model*: modelled as an internal mixture of a water soluble component at 80%
1377 relative humidity (5% by volume), and mineral dust in nucleation (3% by volume),
1378 accumulation (72% by volume), and coarse (20% by volume) modes (Hess et al., 1998); the
1379 dust refractive index for the three modes is that reported by CA80. The region in blue in the
1380 plot indicates the range of variability of the results of this study. The legend in bottom panel
1381 identifies the line styles used in the plot for literature data. Refractive index y-axes are
1382 located on the left side of the plots, with the only exception of LO88 for which the y-axis is
1383 on the right side.
1384

1385 **Figure 8.** Mass extinction efficiency (k_{ext} , $\text{m}^2 \text{ g}^{-1}$), single scattering albedo (ω), and
1386 asymmetry factor (g) computed with the Mie theory between 2.5 and $25 \mu\text{m}$ for the five
1387 analysed dust cases. Calculations have been performed by considering for each sample the
1388 estimated refractive and (left panel, a) the same size distribution for the five cases, i.e. the

1389 mean_B reported in Fig.1, or (right panel, b) the own size distribution measured in
1390 correspondence of each sample. By comparison, also the spectral optical properties obtained
1391 using the OPAC refractive index, calculated considering the mean_B size distribution, are
1392 shown in the plot. The legend in top left panel identifies the line styles used in the plot.

1393

1394 **Figure 9.** Mass extinction efficiency (k_{ext} , $\text{m}^2 \text{ g}^{-1}$) calculated for the five dust cases in the 7.5-
1395 12.5 μm spectral range. According to Fig. 8, continuous and dashed lines corresponds to k_{ext}
1396 calculations performed by considering respectively the same size distribution for all dust
1397 cases (continuous lines) and the own size distribution measured in correspondence of each
1398 sample (dashed lines). Vertical lines and the two shaded areas refers to the following
1399 different satellite remote sensing channels: (grey dashed lines) six AIRS channels for dust
1400 retrieval in the thermal infrared (8.10, 8.15, 9.31, 10.36, 11.48, 11.86); (black dashed line)
1401 IASI channel for dust optical depth retrieval at 10 μm ; (grey shaded areas) the two MODIS
1402 broadband channels (10.78-11.28 and 11.77-12.27 μm) used for Sea Surface Temperature
1403 (SST) estimation.

1404 **Tables**

1405

1406 **Table 1.** Main characteristics of the five dust cases selected in this study: the sample ID, the measurement site, the date and time of beginning
 1407 and end of the observed dust event, the associated filter sampling time interval within the event, and the identified dust source region. The mean
 1408 aerosol optical depth (τ) at 0.50 μm and the Ångstrom exponent (α , calculated between 0.44 and 0.87 μm) obtained from AERONET
 1409 measurements during filter sampling for the different cases are also reported; no data are available for the SOP1-8, when the solar zenith angle at
 1410 the start of the sampling was $>70^\circ$, and for the SOP1-17, which corresponds to nighttime data.

1411

1412

Sample ID	Measurement site	Dust event period: beginning – end (date and time in UTC)	Dust sampling period within the event: beginning – end (date and time in UTC)	Dust source	$\tau_{0.50\mu\text{m}}$ (from AERONET)	$\alpha_{0.44-0.87\mu\text{m}}$ (from AERONET)
SOP0-47	Banizoumbou	09/02/2006 01:50 – 10/02/2006 02:20	09/02/2006 09:28 – 09/02/2006 16:32	Algeria – Niger and Mali – Niger frontier areas	0.52	0.15
SOP1-8	Banizoumbou	04/06/2006 16:52 – 04/06/2006 17:36	04/06/2006 16:52 – 04/06/2006 17:36	Local erosion event	-	-
SOP1-17	Banizoumbou	08/06/2006 22:33 – 09/06/2006 06:40	08/06/2006 22:33 – 09/06/2006 06:40	Local erosion event	-	-
N32	Tamanrasset	21/07/2006 ~21:00 – 27/07/2006 ~18:00	23/07/2006 09:55 – 24/07/2006 11:41	Eastern part of the Algeria – Niger frontier area	1.30	0.06
N93	Tamanrasset	05/10/2006 ~00:00 – 07/10/2006 ~12:00	05/10/2006 13:09 – 07/10/2006 10:40	Algerian Atlas	0.48	0.11

1413

1414

1415

1416

1417

1418 **Table 2.** Mineralogical composition (% by mass) of the five samples from the Banizoumbou and the Tamanrasset sites. The estimated
 1419 uncertainties associated to the identification of the different mineral species are: clays ($\pm 8-20\%$), quartz ($\pm 3\%$), calcite ($\pm 3\%$), dolomite ($\pm 10\%$),
 1420 gypsum ($\pm 5\%$), orthose ($\pm 7\%$), albite ($\pm 2\%$), iron oxides ($\pm 10-12\%$).

1421

Sample ID	Clays			Quartz	Ca-rich			Feldspars		Iron Oxides	
	Kaolinite	Illite	Smectite		Calcite	Dolomite	Gypsum	Orthose	Albite	Hematite	Goethite
SOP0-47	81%	8%	ND	6%	ND	<1%	<1%	<1%	<1%	4%	
SOP1-8	47%	5%	ND	40%	ND	ND	ND	3%	<1%	4%	
SOP1-17	80%	8%	ND	6%	ND	ND	ND	<1%	ND	1%	4%
N32	90%			5%	<1%	ND	<1%	<1%	<1%	4%	
N93				17%	6%	ND	5%	<1%	<1%	4%	

1422 ND = Not Detected

1423

1424 **Table 3.** Position of main detected dust infrared band peaks with associated mineral species
 1425 and transition assignment.

1426

Wavelength (μm)	Wavenumber (cm^{-1})	Mineral specie	Assignment
2.7	3700	kaolinite	OH stretching
2.76	3620	kaolinite	OH stretching
7.0	1431	calcite	$(\text{CO}_3)^{2-}$ stretching
8.8	1135	gypsum	SO_4 stretching
9.0	1117	kaolinite, smectite	Si-O stretching
9.2	1092	quartz	Si-O stretching
9.7	1035	illite, kaolinite, smectite	Si-O stretching
9.9	1008	kaolinite	Si-O stretching
10.9	914	kaolinite	Al-OH deformation
11.4	876	calcite	C-O stretching
12.5	800	quartz	Si-O bending
12.9	777	quartz	Si-O bending
18.8	533	kaolinite	Fe-O, Fe_2O_3 , Si-O-Al stretching
19.3	519	illite, smectite	Al-O-Si deformation
21.4	468	illite, kaolinite, smectite	Si-O-Si bending
23.1	433	illite, kaolinite	Si-O deformation

1427

1428

1429

1430

1431

1432

1433

1434

1435

1436

1437

1438

1439

1440 **Table 4.** Estimated dust optical depth and TOA forcing efficiency (FE, $\text{W m}^{-2} \tau^{-1}$) at 8, 10,
 1441 and 12 μm for the SOP0-47, N32, and N93 cases (see text for details). The measured τ at 0.50
 1442 μm from AERONET is also reported.

1443

		8 μm		10 μm		12 μm	
	$\tau_{0.50\mu\text{m}}$ (from AERONET)	$\tau_{8\mu\text{m}}$	$\text{FE}_{8\mu\text{m}}$	$\tau_{10\mu\text{m}}$	$\text{FE}_{10\mu\text{m}}$	$\tau_{12\mu\text{m}}$	$\text{FE}_{12\mu\text{m}}$
SOP0-47	0.52	0.18	42.6	0.31	25.1	0.20	39.8
N32	1.30	0.36	54.0	0.92	21.2	0.48	40.8
N93	0.48	0.17	43.2	0.31	23.1	0.23	31.1

1444

1445

1446

1447

1448

1449

1450

1451

1452

1453

1454

1455

1456

1457

1458

1459

1460

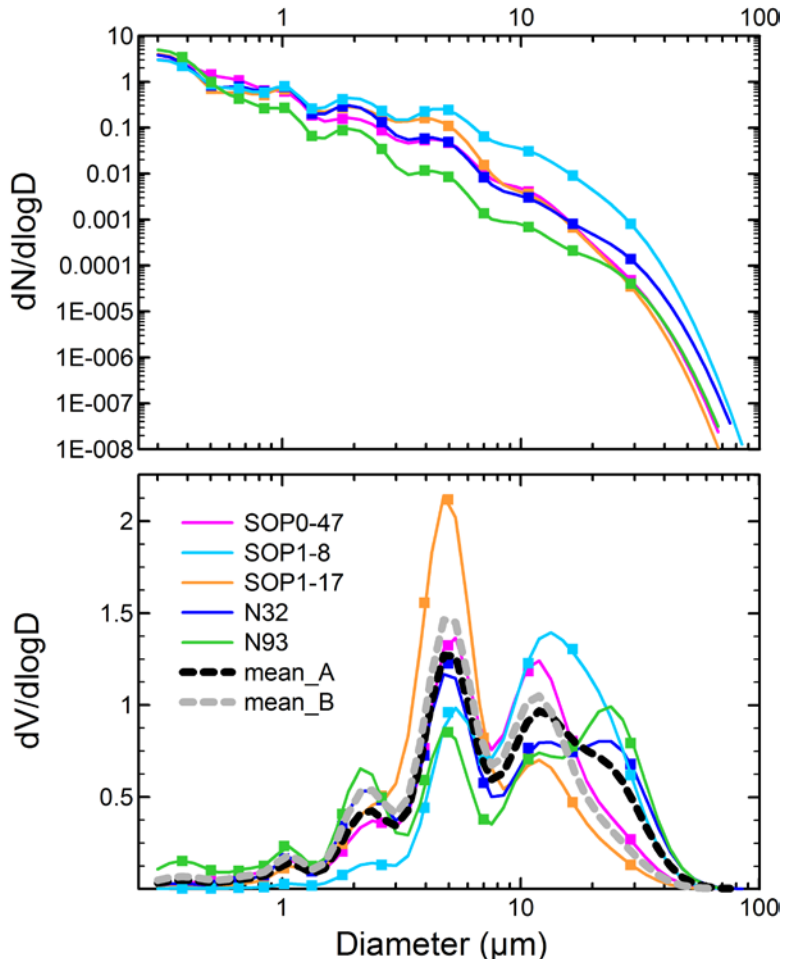
1461

1462

1463

1464 **Figures**

1465 **Figure 1.** Particle number ($dN/d\log D$) and volume ($dV/d\log D$) size distributions (normalized
 1466 with respect to the total number and total volume of particles, respectively) obtained for the
 1467 five selected dust events. The dots indicate the GRIMM measured values, while the lines are
 1468 the multimodal lognormal fits data. Black and grey dashed lines are the averages of the
 1469 volume size distributions for the five samples obtained including (mean_A, black dashed
 1470 line) and excluding (mean_B, grey dashed line) the largest mode at $\sim 25 \mu\text{m}$ for N32 and N93
 1471 samples. The legend in bottom panel identifies the line styles used in the plot.



1472

1473

1474

1475

1476

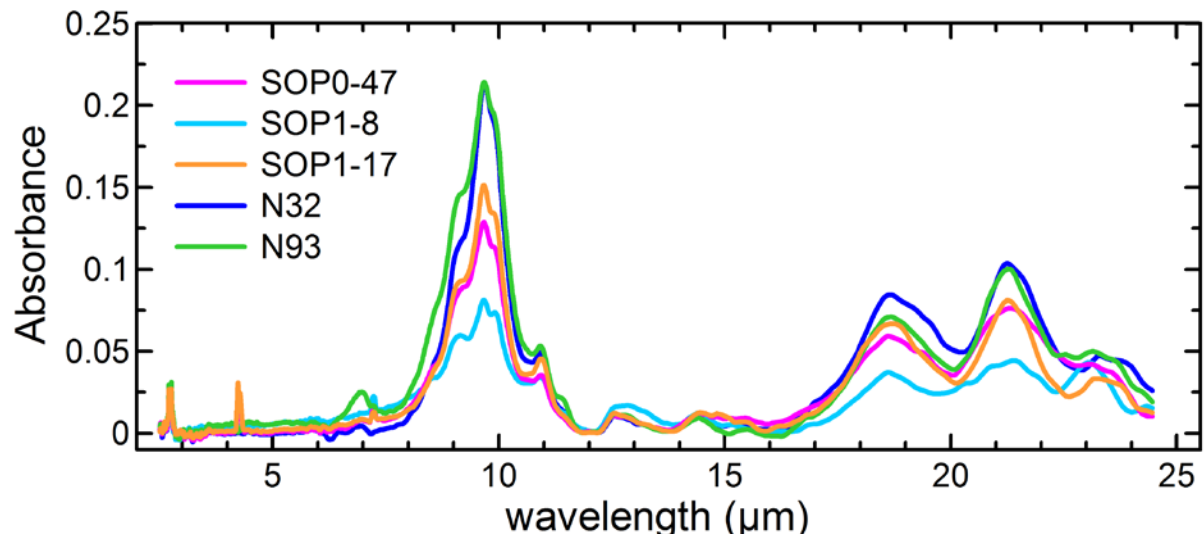
1477

1478

1479

1480 **Figure 2.** Absorbance spectra measured in the spectral range 2.5-25 μm for the five different
1481 dust samples. The legend identifies the line styles used in the plot.

1482



1483

1484

1485

1486

1487

1488

1489

1490

1491

1492

1493

1494

1495

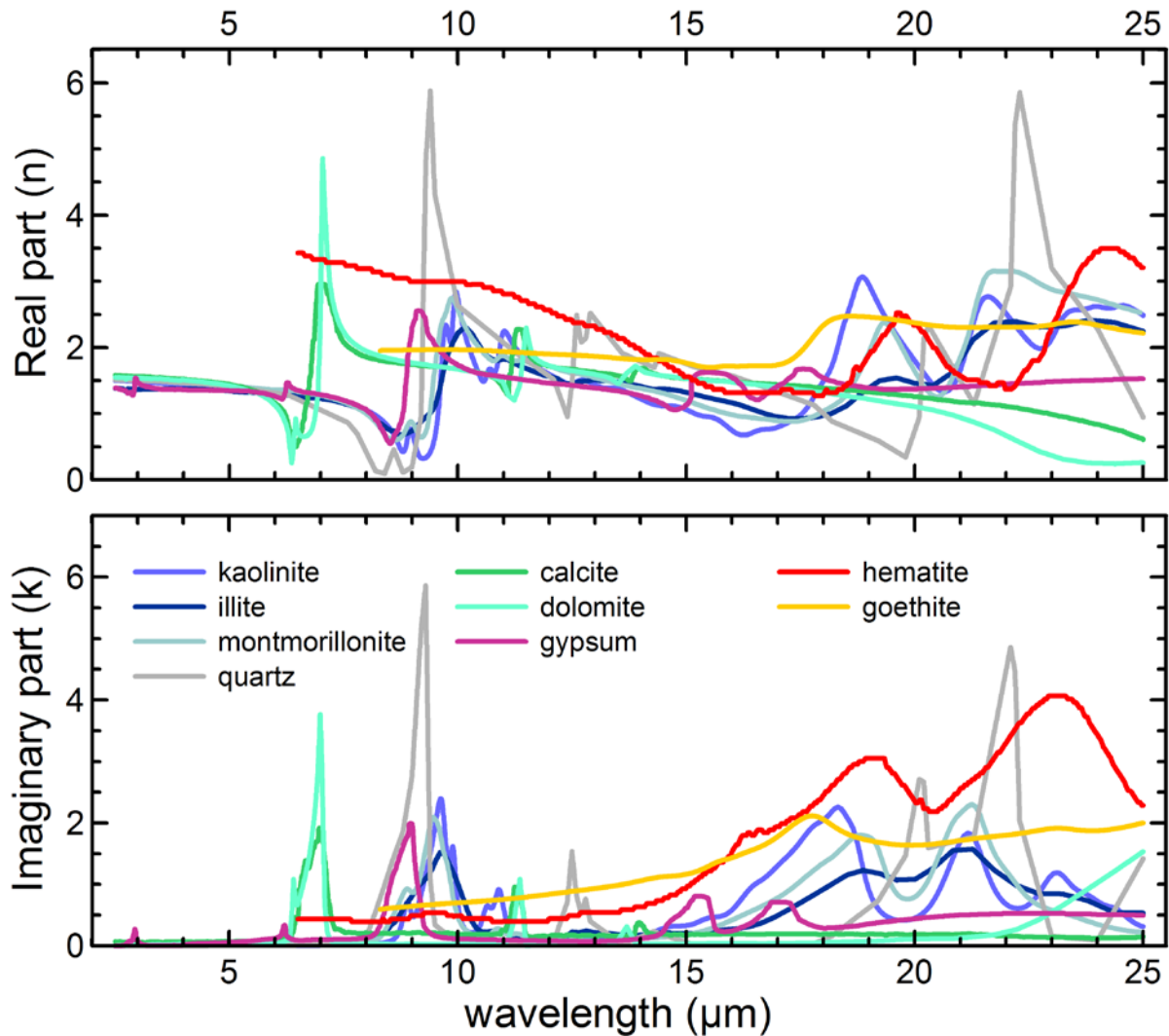
1496

1497

1498

1499

1500 **Figure 3.** Real (n) and imaginary (k) parts of the complex refractive index in the spectral
 1501 range 2.5-25 μm for individual minerals composing dust. References for the plotted curves
 1502 are: kaolinite (Glotch et al., 2007); illite (Querry, 1987); montmorillonite (a mineral of the
 1503 smectite family, taken here as representative for this clay species) (Glotch et al., 2007);
 1504 quartz (Peterson and Weiminan, 1969); calcite (Querry et al., 1978; Long et al., 1993);
 1505 dolomite (Querry, 1987); gypsum (Long et al., 1993); hematite (Marra et al., 2005); goethite
 1506 (Glotch and Rossman, 2009). No literature data are available for feldspars (orthose and
 1507 albite) at infrared wavelengths. The colour code used for the different minerals is indicated in
 1508 the legend.



1509

1510

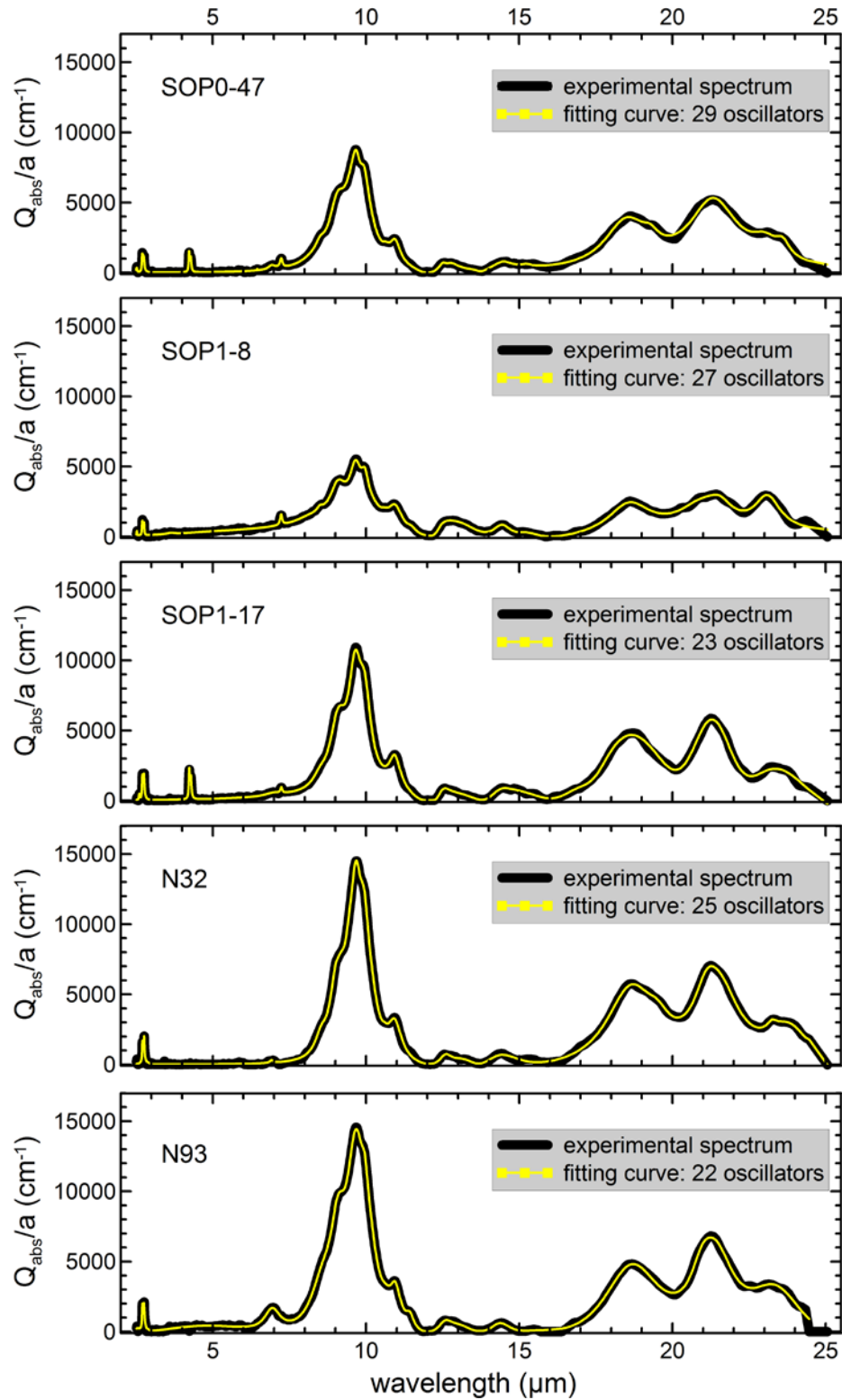
1511

1512

1513

1514

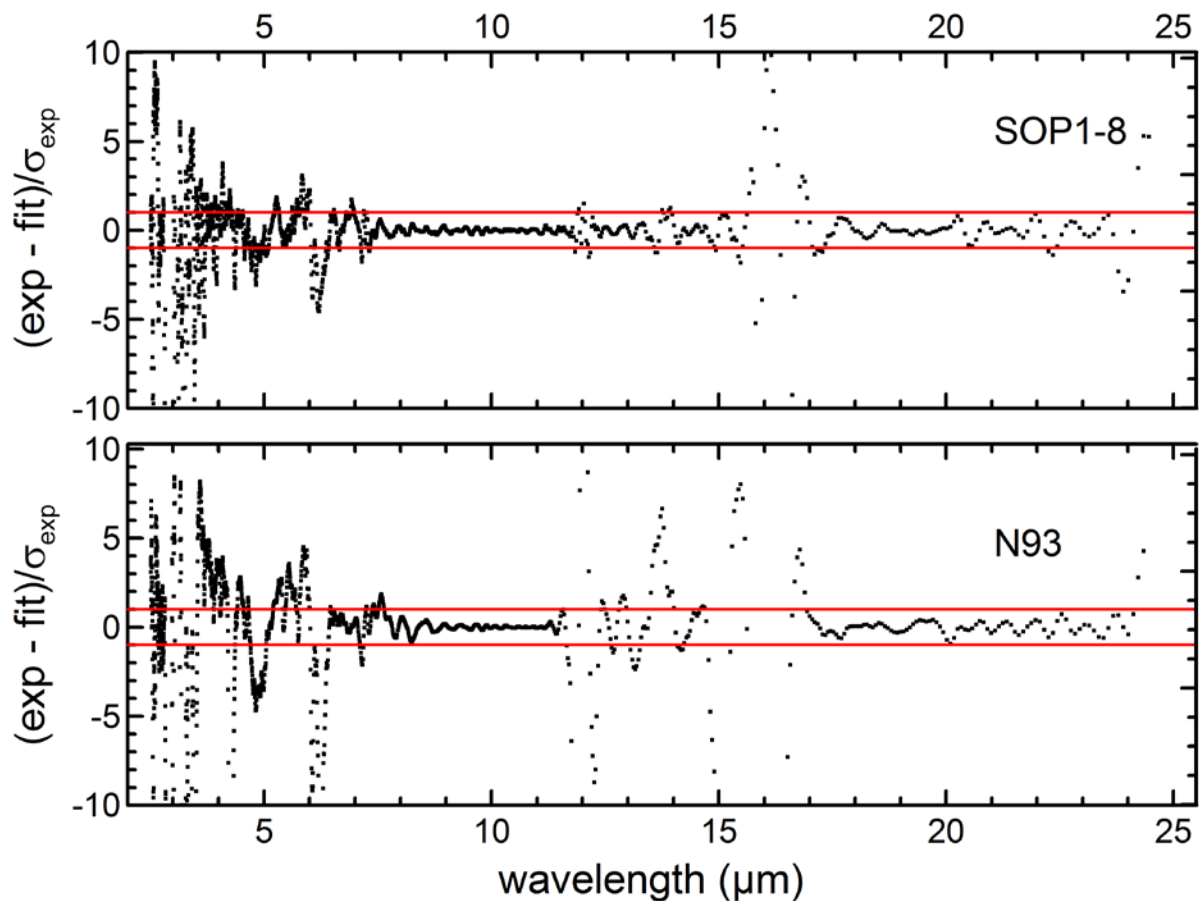
1515 **Figure 4.** Comparison between the experimental $Q_{\text{abs}}(\lambda)/a$ (cm^{-1}) spectra (black curves) and
 1516 the theoretical ones obtained from the nonlinear fitting procedure (yellow curves). The line
 1517 styles used in the plot and the number of oscillators for each fit are also indicated in the
 1518 legend.



1519

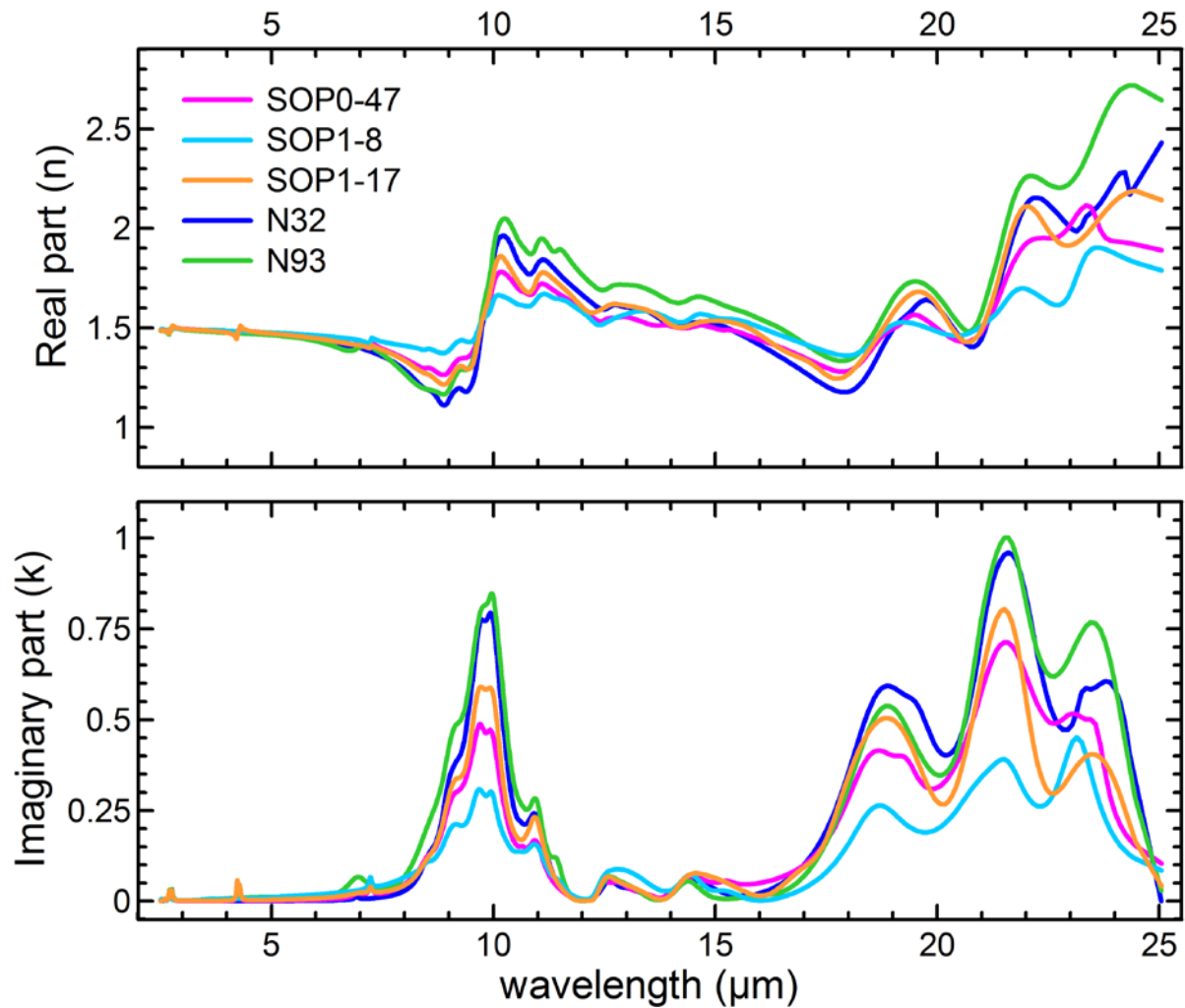
1520

1521 **Figure 5.** Residuals ($R = \frac{(\text{exp} - \text{fit})}{\sigma_{\text{exp}}}$) of the fit normalized by the measurement errors
1522 calculated for SOP1-8 and N93. In the residual calculation, exp is the experimental $Q_{\text{abs}}(\lambda)/a$,
1523 while fit is the $Q_{\text{abs}}(\lambda)/a$ obtained from the fitting procedure. The measurement error, σ_{exp} , is
1524 6.4% for SOP1-8 and 5.9% for N93. Red lines indicate the ± 1 interval.



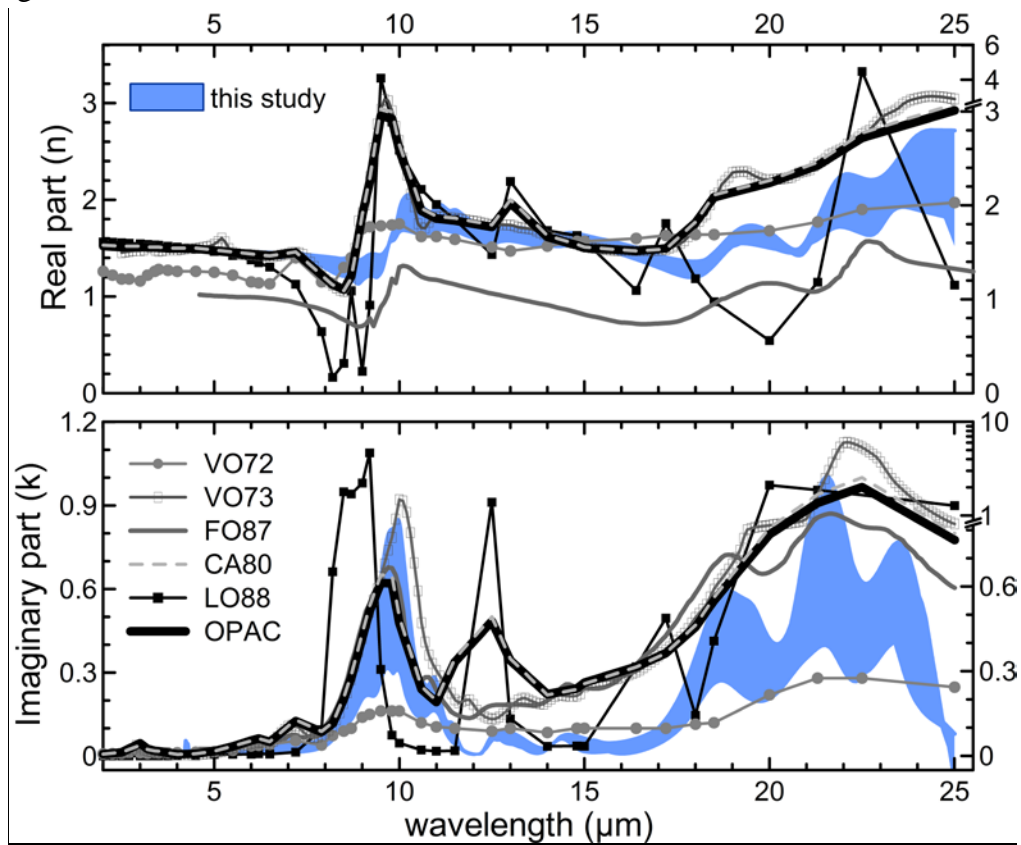
1536 **Figure 6.** Real (n, top panel) and imaginary (k, bottom panel) part of the complex refractive
1537 index obtained in the range $2.5 - 25 \mu\text{m}$ for the five different dust samples. The legend
1538 identifies the line styles used in the plot.

1539
1540



1541
1542
1543
1544
1545
1546
1547
1548
1549

1550 **Figure 7.** Comparison of our results with other direct and indirect estimates of the dust
 1551 refractive index as reported in the literature. The plot reports the real and the imaginary parts
 1552 of the refractive index for: 1. *Volz (1972)* (indicated as VO72 in the plot): rainout dust
 1553 aerosols collected in Germany and composed of a mixture of soil particles, fly ashes, and
 1554 pollen (spectroscopy method; also used as the “dust-like” model in Shettle and Fenn, 1979);
 1555 2. *Volz (1973)* (indicated as VO73): Saharan dust collected at Barbados, West Indies
 1556 (spectroscopy method); 3. *Fouquart et al. (1987)* (indicated as FO87): Saharan sand collected
 1557 at Niamey, Niger (spectroscopy method); 4. *Carlson and Benjamin, (1980), Sokolik et al.*
 1558 (*1993*) (indicated as CA80): mineral dust model, as used in the OPAC and GADS databases
 1559 (based on a synthesis of measurements on Saharan dust or generally on desert aerosols); 5.
 1560 *Longtin et al. (1988)* (indicated as LO88): dust sand, i.e. modelled as an internal mixture of
 1561 hematite (10% by volume) and quartz. In the internal mixing hypothesis the dust refractive
 1562 index is calculated as the volume average of the refractive indices of individual minerals; 6.
 1563 *OPAC desert model*: modelled as an internal mixture of a water soluble component at 80%
 1564 relative humidity (5% by volume), and mineral dust in nucleation (3% by volume),
 1565 accumulation (72% by volume), and coarse (20% by volume) modes (Hess et al., 1998); the
 1566 dust refractive index for the three modes is that reported by CA80. The region in blue in the
 1567 plot indicates the range of variability of the results of this study. The legend in bottom panel
 1568 identifies the line styles used in the plot for literature data. Refractive index y-axes are
 1569 located on the left side of the plots, with the only exception of LO88 for which the y-axis is
 1570 on the right side.

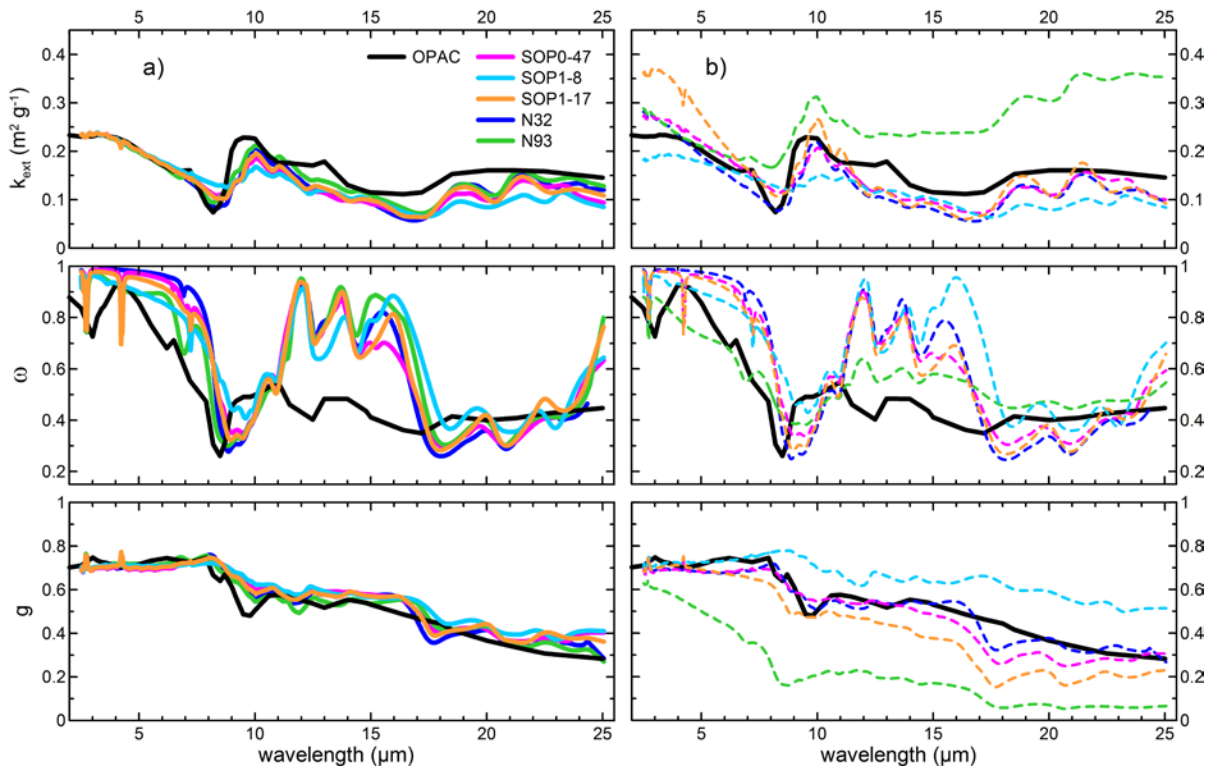


1571

1572

1573 **Figure 8.** Mass extinction efficiency (k_{ext} , $\text{m}^2 \text{ g}^{-1}$), single scattering albedo (ω), and
 1574 asymmetry factor (g) computed with the Mie theory between 2.5 and 25 μm for the five
 1575 analysed dust cases. Calculations have been performed by considering for each sample the
 1576 estimated refractive and (left panel, a) the same size distribution for the five cases, i.e. the
 1577 mean_B reported in Fig.1, or (right panel, b) the own size distribution measured in
 1578 correspondence of each sample. By comparison, also the spectral optical properties obtained
 1579 using the OPAC refractive index, calculated considering the mean_B size distribution, are
 1580 shown in the plot. The legend in top left panel identifies the line styles used in the plot.

1581



1582

1583

1584

1585

1586

1587

1588

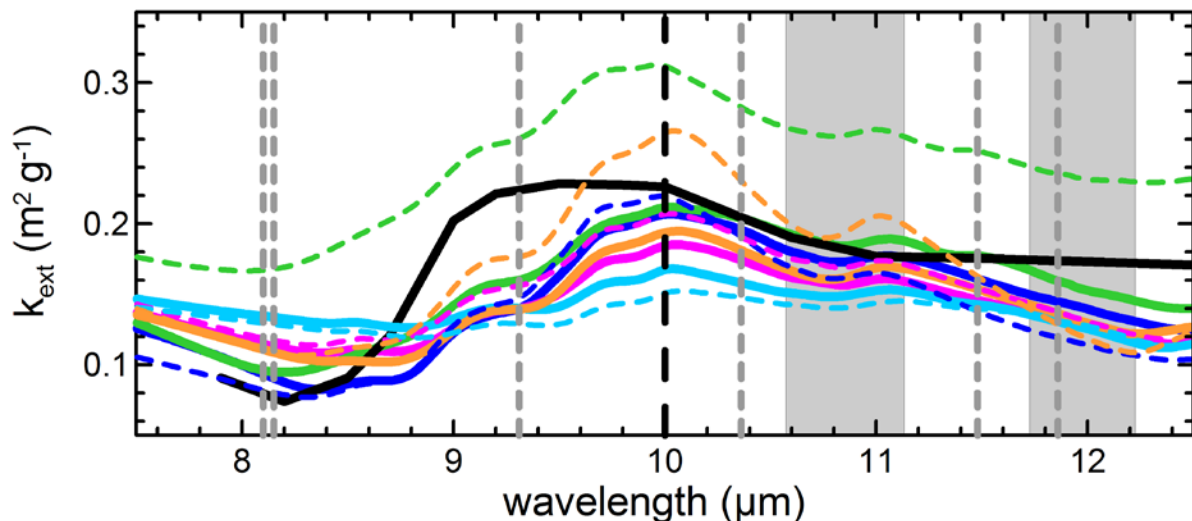
1589

1590

1591

1592 **Figure 9.** Mass extinction efficiency (k_{ext} , $\text{m}^2 \text{ g}^{-1}$) calculated for the five dust cases in the 7.5-
 1593 12.5 μm spectral range. According to Fig. 8, continuous and dashed lines corresponds to k_{ext}
 1594 calculations performed by considering respectively the same size distribution for all dust
 1595 cases (continuous lines) and the own size distribution measured in correspondence of each
 1596 sample (dashed lines). Vertical lines and the two shaded areas refers to the following
 1597 different satellite remote sensing channels: (grey dashed lines) six AIRS channels for dust
 1598 retrieval in the thermal infrared (8.10, 8.15, 9.31, 10.36, 11.48, 11.86); (black dashed line)
 1599 IASI channel for dust optical depth retrieval at 10 μm ; (grey shaded areas) the two MODIS
 1600 broadband channels (10.78-11.28 and 11.77-12.27 μm) used for Sea Surface Temperature
 1601 (SST) estimation.

1602



1603